DISSERTATIONES
CHIMICAE
UNIVERSITATIS
TARTUENSIS
175

OVE OLL

Electrical double layer structure and energy storage characteristics of ionic liquid based capacitors

DISSERTATIONES CHIMICAE UNIVERSITATIS TARTUENSIS
175

DISSERTATIONES CHIMICAE UNIVERSITATIS TARTUENSIS
175

OVE OLL

Electrical double layer structure and energy storage characteristics of ionic liquid based capacitors

UNIVERSITY OF TARTU
Press

Institute of Chemistry, Faculty of Science and Technology, University of Tartu, Estonia

The dissertation is accepted for the commencement of the degree of Doctor of Philosophy in Chemistry on 21st June, 2018 by the Council of Institute of Chemistry, University of Tartu.

Supervisors: Ph.D. Tavo Romann, University of Tartu, Estonia

Prof. Enn Lust, University of Tartu, Estonia

Opponent: Prof. Dr. Helmut Baltruschat, University of Bonn, Germany

Commencement: August 27, 2018 at 14:15, Ravila Street 14a–1020, Tartu (Chemicum)

ISSN 1406-0299
ISBN 978-9949-77-806-5 (print)
ISBN 978-9949-77-807-2 (pdf)

University of Tartu Press
www.tyk.ee

TABLE OF CONTENTS

1. LIST OF ORIGINAL PUBLICATIONS

I T. Romann, **O. Oll**, P. Pikma, E. Lust, Abnormal infrared effects on bismuth thin film–EMImBF$_4$ ionic liquid interface, Electrochem. Commun. 23 (2012) 118–121.

II T. Romann, **O. Oll**, P. Pikma, H. Tamme, E. Lust, Surface chemistry of carbon electrodes in 1-ethyl-3-methylimidazolium tetrafluoroborate ionic liquid–an in situ infrared study, Electrochimica Acta. 125 (2014) 183–190.

III **O. Oll**, T. Romann, E. Lust, An infrared study of the few-layer graphene│ionic liquid interface: Reintroduction of *in situ* electro-reflectance spectroscopy, Electrochem. Commun. 46 (2014) 22–25.

IV **O. Oll**, T. Romann, P. Pikma, E. Lust, Spectroscopy study of ionic liquid restructuring at lead interface, J. Electroanal. Chem. 778 (2016) 41–48.

V **O. Oll**, T. Romann, C. Siimenson, E. Lust, Influence of chemical composition of electrode material on the differential capacitance characteristics of the ionic liquid│electrode interface, Electrochem. Commun. 82 (2017) 39–42.

VI T. Romann, **O. Oll**, P. Pikma, K. Kirsimäe, E. Lust, 4–10 V capacitors with graphene-based electrodes and ionic liquid electrolyte, J. Power Sources. 280 (2015) 606–611.

VII T. Romann, E. Lust, **O. Oll**, Method of Forming a Dielectric Through Electrodeposition on an Electrode for a Capacitor, WO/2016/050761, 2016.

VIII **O. Oll**, C. Siimenson, K. Lust, G. Gorbatovski, E. Lust, Specific adsorption from an ionic liquid: impedance study of iodide ion adsorption from a pure halide ionic liquid at bismuth single crystal planes, Electrochimica Acta. 247 (2017) 910–919.

Author's contribution:

Paper I: Performed electrochemistry and surface infrared measurements. Collaborated in experimental data interpretation and participated in manuscript preparation.

Paper II: Performed electrochemistry and surface infrared measurements. Collaborated in experimental data interpretation and participated in manuscript preparation.

Paper III: Performed all electrochemistry and surface infrared measurements and data analysis. Main person responsible for data interpretation and manuscript preparation.

Paper IV: Performed all electrochemistry and surface infrared measurements and data analysis. Main person responsible for data interpretation and manuscript preparation.

Paper V: Performed all electrochemistry measurements and data analysis. Main person responsible for data interpretation and manuscript preparation.

Paper VI: Performed some of the electrochemistry and surface infrared measurements. Collaborated in data interpretation.

Paper VII: The author's share of the patent is 20%.

Paper VIII: Performed all electrochemistry measurements and data analysis. Main person responsible for data interpretation and manuscript preparation.

2. ABBREVIATIONS AND SYMBOLS

AC	alternating current
aC	amorphous carbon
AFM	atomic force microscopy
ATR	attenuated total reflection
BMPyrrDCA	1-butyl-1-methylpyrrolidinium dicyanamide
C	differential capacitance
C_{dl}	electrical double layer capacitance
C_{min}	capacitance minimum
C_{pseudo}	pseudo-capacitance
C_S	series differential capacitance
c	concentration
C(0001)	basal plane of highly orientated pyrolytic graphite
CDC(TiC)	titanium carbide derived carbon
C, E	capacitance *vs.* electrode potential curve
CV	cyclic voltammetry
D	diffusion coefficient
DC	direct current
E	electrode potential
E_{dip}	electroreflectance absorption peak energy
E_F	Fermi level energy
E_{min}	potential at capacitance minimum
$E_{\sigma=0}$	potential of zero total charge
$E(t)$	potential at time t
EC	equivalent circuit
EDL	electrical double layer
EIS	electrochemical impedance spectroscopy
$EMImBF_4$	1-ethyl-3-methylimidazolium tetrafluoroborate
ER	electroreflectance
F	Faraday constant
f	frequency in Hz
Fc	ferrocene
FTIR	Fourier transform infrared spectroscopy
hkl	Miller indices
HOPG	highly oriented pyrolytic graphite
I	electrode current
I_A	current amplitude
i	imaginary unit ($\sqrt{-1}$)
I(t)	current at time t
IR	infrared
IRAS	infrared absorption spectroscopy
IRRAS	infrared reflection absorption spectroscopy
IL	ionic liquid

j	electrode current density
m	mass of a particle
MD	molecular dynamics
n	number of electrons
n_{mol}	number of moles of electrons
PDCA	polydicyanamide
PMImI	1-propyl-3-methylimidazolium iodide
pzc	potential of zero charge
Q	electric charge
R_{ad}	adsorption resistance
R_{ct}	charge transfer resistance
R_D	diffusion resistance
RF	radio-frequency
rms	root mean square roughness
RTIL	room temperature ionic liquid
S	surface area of the electrode
SC	supercapacitor
SEIRA	surface enhanced infrared absorption
STM	scanning tunneling microscopy
t	time
UHV	ultra high vacuum
XRD	X-ray diffraction
Z	impedance
Z'	real part of impedance
Z''	imaginary part of impedance
Z_W	Warburg−like finite−length diffusion impedance
$\delta c_{red}/\delta x$	reduced species concentration gradient
μ	molecular dipole moment
v	potential scan rate
π	Pi number
Φ	phase angle shift
χ^2	chi−square function
ω	angular frequency

3. INTRODUCTION

Electrochemical energy storage and conversion devices are the basis of a sustainable energy economy of the future. Whether it is solar cells that convert electromagnetic radiation into electrical energy, fuel cells that consume chemical energy to power transportation, electrolysis cells that convert water into fuel, secondary batteries powering consumer electronics, supercapacitors that deliver considerable energy savings for high-power applications or dielectric capacitors that allow for efficient conversion between AC and DC signals, we are surrounded by advanced electrochemical devices. The active part of all of these devices is the interface between two dissimilar phases, where all the electrochemical reactions take place and energy is stored. In order to design more efficient electrochemical devices, however, detailed knowledge of this interface is of vital importance. This thesis focuses specifically on capacitive energy storage devices and the difference between purely electrostatic-, dielectric- and pseudo-capacitors from the perspective of their interfacial behaviour in ionic liquid electrolytes.

Ionic liquids (ILs) are a class of low-temperature liquid phase salts. Interest in ILs is centred around the ability to tune the properties of an IL by varying the chemical composition of both the cation and anion that compose the IL. In such a way it is possible to derive a mixture that has the desired physical and chemical properties for the specific application in mind. For example, many electrochemical systems require electrolytes to have high ionic conductivity, low viscosity and high electrochemical stability for efficient use, which ILs can deliver [1]. Other devices, such as dye-sensitized solar cells, require the electrolyte to be electrochemically reactive but stable to atmospheric moisture, also achieved by ILs [2]. Such versatility is also utilised in this work examining the electrochemical behaviour of three different ILs for application in electrochemical energy storage.

The main aims of the thesis are to:

a) Derive an advanced understanding of the processes that govern the electrical double layer formation between an ionic liquid and electrodes of variable electronic properties [I–V]
b) Understand the energy storage mechanism of polydicyanamide based dielectric capacitors [VI–VII]
c) Study the mechanism of iodide ion specific adsorption from an ionic liquid at different bismuth single crystal planes [VIII]

Both classical electrochemical measurements, physical characterization methods as well as *in situ* infrared spectroscopy are employed in order to understand the mechanism of energy storage at IL│electrode interfaces and design more efficient and higher specific energy electrochemical devices for the future.

4. LITERATURE OVERVIEW

4.1. Electrical double layer

The formation of the electrical double layer (EDL) is based on the Volta problem [3]. When two phases of dissimilar electric potentials intersect, a layer is formed at the interface between the two materials that controls the drop in electric potential between the two phases, consuming energy in the process. The EDL is always neutral, but can have a considerable amount of electric charge built up within the separate phases, which amounts to the energy stored within the EDL. The storage of electrostatic energy within the EDL has been a matter of scientific curiosity since the invention of the Leyden jar in 1745 [4]. By observing that the capacitance of the device is linearly dependent on the dielectric property of the insulator and inversely proportional to the thickness of the insulator, Helmholtz [5] proposed the first model for the EDL in electrolyte solutions, proposing a double layer model of opposite charges on separate sides of the interface with a constant, linear decrease of potential between the layers, which adequately describes the behaviour of dielectric capacitors. In order to explain specific experimental data for electrode | electrolyte interfaces, many models have been developed over the 20th century to account for specific differences in EDL behaviour. Gouy and Chapman [6,7] studied the surface energy of Hg in dilute aqueous electrolyte solutions while Stern [8] improved upon their effort to also consider more concentrated electrolytes. Rice [9] first proposed the dependence of EDL capacitance on electronic properties of the electrode. Frumkin [10] and Grahame [11] first considered the effects of chemical interaction on the EDL formation in specifically adsorbing media. Finally, Gerischer [12,13] introduced effects of semi-conductor and semi-metal electrodes to the volume of EDL theories [14]. All these theories fundamentally describe charged phases of a single interface, while electrochemical systems always constitute of at least two interfaces in order for polarization of the system to be changed. Thus it should be no surprise that the EDL exists even when there is no charge within either phase, the potential of zero charge (pzc), in direct contradiction with the original definition of a “double layer” [5]. This is primarily because the absence of charge does not imply an absence of electrical potential difference between the phases in contact. Indeed, the work function of metals is significantly higher than that of dielectric materials [14], which means that electrons are more stabilized in the conductive phase than the dielectric phase, with the difference amounting to the electrochemical work function.

It has been shown that within the limitation of ideal polarizability, the pzc well correlates with the electronic work function of single crystal metal planes [15]. The EDL thus describes an interfacial region that limits electrons from crossing the interfacial barrier, being limited by the oxidation potential in the positive polarization range and reduction potential in the negative polarization range. The difference between these two potentials is called the ideal polarizability potential range and is a property of a combination of electrode and electrolyte.

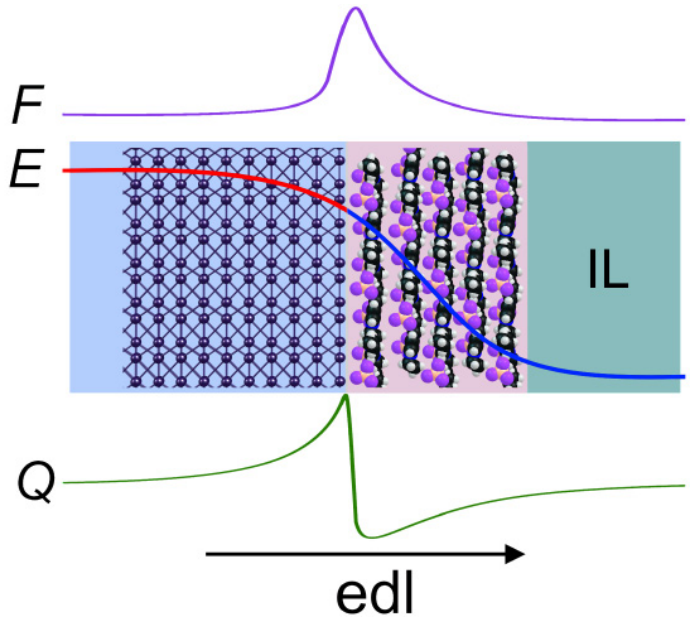

Figure 1. Schematic of the electrical double layer at electrode | ionic liquid interface with major physical parameters electric field strength *F*, potential *E* and charge *Q*.

Fig. 1 shows a model of the interface between an electrode and an IL electrolyte also showing the dependence of major physical parameters characteristic to the EDL. In ILs the dependence of capacitance on electrode potential is often described by the mean-field theory based model by Kornyshev [16]. The model is loosely based [17] on the derivations of the Gouy-Chapman-Stern model, with added consideration for finite ion size and a free parameter describing the compressibility of an IL. Different from models developed for electrolyte solutions, the model by Kornyshev shows the *C, E* curve having a maximum at the pzc, with the capacitance decreasing with either positive or negative polarization, explained by effects of lattice saturation and overscreening [18]. In order to better describe experimental observations [19–26] of the capacitance-potential dependence of the EDL in ILs, many additional modelling [27–34] and theoretical [16,18,35–39] considerations have been published and reviewed [40,41].

4.2. Ionic liquids

ILs are a class of ionic, salt-like materials that are liquidous at low temperatures. The official definition of ILs uses the boiling point of water as a point of reference: “Ionic liquids are ionic compounds which are liquid below 100 °C” [42]. In particular, salts that are liquids at room temperature are called room temperature ionic liquids (RTIL). RTILs are a class of non-molecular

ionic solvents with low melting points. The accepted definition of an RTIL is any salt that has a melting point lower than 20-25°C [40,42].

The first RTIL was reported by Walden in 1914 [43]. It was based on the ethylammonium cation and nitrate anion. Thereafter, many ILs containing a variety of cations and anions of different sizes have been synthesized for specific applications. Air- and water-stable ILs are increasingly employed to replace organic solvents in a variety of chemical processes due to their non-volatile, non-flammable nature, and in some cases, stability at temperatures over 400 °C [44].

ILs have mediocre ionic conductivities compared with those of organic solvents/electrolyte systems (up to 30 mS cm^{-1}). At elevated temperatures, for example 200 °C, a conductivity above 0.1 S cm^{-1} can be achieved for some ILs. However, at room temperature their conductivities are lower than those of concentrated aqueous electrolytes. Because ILs are composed entirely of ions, it would be expected that ionic liquids have high ionic conductivities. This is not the case since the conductivity of any solution depends not only on the number of charge carriers but also on their mobility. The large constituent ions of ILs reduce the ion mobility which, in turn, leads to lower conductivity. Furthermore, ion aggregation leads to higher viscosity. The conductivity of ILs is inversely related to their viscosity [45].

Generally, ILs are more viscous than common organic solvents and their viscosities range from 10 mPa·s to above 1 Pa·s at room temperature. The viscosity of ILs is determined by van der Waals forces and hydrogen bonding. Electrostatic interactions also play an important role. Alkyl chain lengthening in the cation leads to an increase in viscosity due to stronger van der Waals forces between the alkyl chains of cations, leading to increase in the energy required for molecular motion, or even formation of aggregates. Also, the ability of anions to form hydrogen bonds has a pronounced effect on viscosity [45,46].

Most ILs have higher density than water with values ranging from 0.9 for typical ILs to 1.6 g cm^{-3} for ILs with bulky anions. Density strongly depends on the size of the cycle in the cation, on the length of the alkyl chains of the cation, the symmetry of ions and on the interaction forces between the cations and the anions. ILs with aromatic head rings, in general, present greater densities than pyrrolidinium head ring ILs and piperidinium ring ILs. Density also increases with the increase of symmetry of the cations [42].

Ionic liquids can be thermally stable up to temperatures of 400 °C, however, the absolute thermal stability is usually overestimated due to kinetic limitations in IL decomposition. The thermal stability of ionic liquids is limited by the strength of their heteroatom-carbon bonding, their heteroatom–hydrogen bonds and basicity of the anion. Long exposure of ILs to high temperatures can lead to radical decomposition. Most ILs have extremely low vapour pressures, which enables water removal by heating under vacuum [45,47].

The electrochemical stability range of an electrolyte is the electrochemical potential range within which the electrolyte is neither reduced nor oxidized at a passive electrode. This value determines the electrochemical stability of a

dielectric media. ILs have significantly wider electrochemical stability ranges than aqueous electrolytes, hence the dual usability as both solvent and electrolyte has opened interesting possibilities in the field of fundamental and applied electrochemical studies. For instance, ILs have been already used as electrolytes in capacitors, electrodeposition of metals and alloys, electrocatalysis and energy storage devices and for optimizing the heterogeneous reaction mechanism [48,49].

Due to RTILs high stability under applied potential, low vapour pressure, excellent thermal stability, good ionic conductivity, non-flammable and tuneable properties, the RTIL | electrode interface attracts considerable attention, determining the characteristics of various electrochemical energy storage and conversion devices, including secondary batteries, fuel cells and dye-sensitized solar cells [48–52]. RTILs are considered as possible electrolytes for gas sensing applications, since their favourable properties (low-volatility, high thermal stability, good gas solubility) mean that the sensor does not dry out, and provides the possibility for gas sensing at high temperatures [53].

In 1992, Wilkes and Zaworotko reported the first air and moisture stable ionic liquids based on 1-ethyl-3-methylimidazolium cation with either tetrafluoroborate or hexafluorophosphate anion [54]. Although the melting point of 1-ethyl-3-methylimidazolium tetrafluoroborate ($EMImBF_4$) (13 °C) is too high for many practical applications, it is a widely used RTIL for analysing the influence of the chemical nature of different metal electrodes on the RTIL | interface parameters [26,55–63]. Problems with viscosity and conductivity can be overcome via mixing of different ILs or by small additions of organic solvents [64–66]. Table 1 outlines some of the major physical parameters of the ILs applied in this thesis.

Table 1. Physical parameters of the applied ionic liquids at room temperature.

Ionic liquid	Density / g cm^{-3}	Viscosity / mPa·s	Melting point / °C	Conductivity / mS cm^{-1}
$EMImBF_4$	1.28	37	13	14
BMPyrrDCA	0.95	50	−55	12.4
PMImI	1.54	880	-	0.58

Ref. [67–71]

4.3. *In situ* infrared absorption spectroscopy

Over the last two decades, *in situ* infrared (IR) spectroelectrochemistry has become an increasingly applied analytical method in electrochemistry, and has developed strongly in terms of the diversity of electrochemical systems that have been studied. This transition may be associated with the ready availability

of relatively inexpensive, research grade Fourier transform infrared (FTIR) spectrometers. In contrast to the early 1980s, the detection of organic monolayers is now commonplace and there are other exciting works in fields such as organometallic spectroelectrochemistry, in-depth studies of the EDL, time-resolved electrokinetic studies, electrocatalysis as a function of potential and the semiconductor │electrolyte interface [72–75].

IR spectroscopy is an analytical technique for chemical compound identification. This is because different chemical functional groups absorb infrared radiation at different wavelengths, dependent upon the nature of the particular chemical bonding within the groups present. The method is relatively fast, sensitive, easy to handle and provides many different sampling techniques for gases, liquids and solids. Important aspects are the convenient qualitative and quantitative evaluation of the spectra [72,76–78]. IR spectroscopy is typically operated in the Mid-IR range between 4000-400 cm^{-1} when it is used for chemical compound identification.

The IR spectral region comprises fundamental vibrations of bound atoms. Whenever such bound atoms absorb infrared radiation, they vibrate, exhibiting IR absorption bands. The condition for a normal vibration *j* to be IR active is a change in molecular dipole moment μ during the vibration:

$$\mu_j = \mu_0 + \left(\frac{\delta\mu}{\delta q_j}\right) q_j + \frac{1}{2}\left(\frac{\delta^2\mu}{\delta q_j^2}\right) q_j^2 + \cdots \quad (1)$$

where q is the normal coordinate describing the motion of atoms during a normal vibration. With respect to the direction of the vibrational movement, we may distinguish between stretching vibrations (changes of bond lengths) and deformation vibrations (changes of bond angles). Deformation vibrations may be subdivided into different bending, twisting, wagging and rocking modes. Subdivision for stretching vibrations refer to the symmetry of the motion (symmetric or asymmetric, in-plane or out-of-plane vibrations) [76].

Fourier Transform (FT) is a mathematical conversion that allows to measure the entire IR spectrum signal simultaneously, afterwards converting the measurement results mathematically into a wavenumber *vs.* transmission spectrum. The relative simplicity of the resulting FTIR analytical methods allows it to be widely used for the analysis of a range of different materials. It is often used in the packaging industry to analyse monomeric materials for purity, and to identify polymers (polyethylene, polyester, nylon) and their compositions [77].

The advantages of FTIR include high throughput, multiplex advantage, better signal-to-noise ratio and precise wavenumber measurement. The major disadvantage of FTIR is the appearance of features present on the spectrum of a sample that are not from the sample. Common examples of artefacts in FTIR spectra include water vapour and carbon dioxide peaks [76].

The non-electrochemical surface enhanced IR absorption effect was first reported by Hartstein and co-workers in 1980 [79]. Osawa *et al.* pioneered the application of this technique for *in situ* electrochemical IR studies on metal thin

films [73,80]. Surface enhanced infrared absorption spectroscopy (SEIRAS) spectra show marked enhancement of the infrared absorption of adsorbed species, up to 100 times that expected on a smooth, bulk metal electrode. A thin metal overlayer excites surface plasmon polaritons of the metal film, the strong electromagnetic fields associated with this excitation provide a sensitive probe of the metal | electrolyte interface, with high enhancement in sensitivity being claimed over the more conventional infrared reflection absorption spectroscopy (IRRAS) method [72].

The mechanism has two distinct parts that complement each other to give the large enhancement that is observed. The major contributor is the electro-magnetic mechanism. This is the effect of the source radiation exciting surface plasmons of the metal surface. This then causes the molecules that have their vibrational dipole moments in line with the electric field absorb more of the energy from the source radiation [73,81].

The other contributors are the chemical interactions. The only one well known is the effect of chemisorption. If the molecules are chemisorbed then resonance coupling with the electric field is induced on the surface of the metal, resulting in a much higher enhancement factor. If they are electrostatically adsorbed, no resonance coupling can take place. There seem to be other chemical interactions occurring as the calculated enhancement effects are still a factor of too low [73].

The application of SEIRA to electrochemistry is very wide. The one example that was discussed was using SEIRA to help determine the mechanism of irreversible electrochemical reactions. However, SEIRA can also be used to probe the structure of the EDL at the electrochemical interface. This is significant because it helps to understand electrocatalytic reactions and energy storage processes. Also, microsecond time resolved monitoring of reversible reactions is possible [60,82–86].

Both the electrolyte and the metal thin film will damp the evanescent wave of reflecting IR radiation by absorbing energy from it. Hence, it is crucial to ensure that the metal working electrode layer, whilst being thick enough to ensure metallic conduction, is not too thick for the evanescent wave to reach the electrode | electrolyte interface [72].

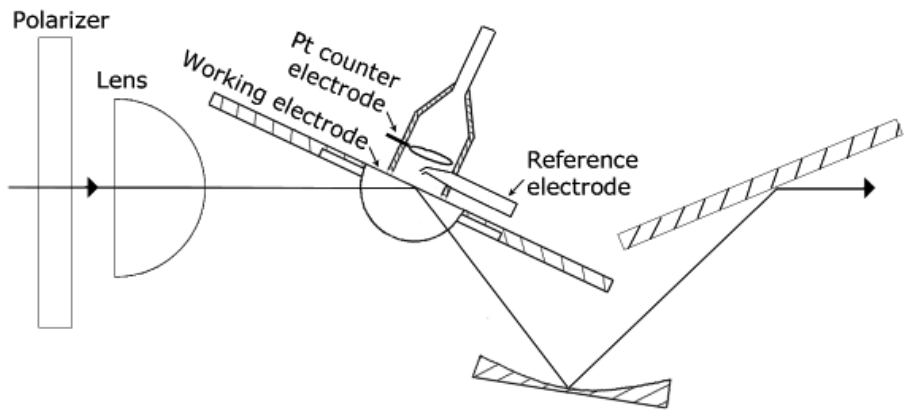

Figure 2. Constructed variable angle (45-65 degrees) *in situ* IR spectroelectrochemical cell with corresponding IR beam path.

The application of SEIRAS (Fig. 2) experiments at solid │liquid interfaces with well-defined metal thin films deposited onto highly refractive, IR-transparent substrates has several advantages in comparison to IRRAS studies, employing the so-called thin electrolyte film configuration (1 to 5 μm) between the optical window and the working electrode: high and specific surface sensitivity with an enhancement of signal up to 100 times stronger compared to IRRAS measurements; dominant first layer signal enhancement effect (compact layer region) with a short decay length of the enhancement field up to 3 to 4 nm toward the electrolyte bulk; signal from the interface and solution background are of comparable magnitude and can be separated by applying a potential modulation method and no severe limitations for mass transport and potential perturbation arise [82,87].

Osawa approximated the polarizability of different metals as well as their dielectric functions:

$$\alpha = \left\{ \frac{(\varepsilon_d - \varepsilon_{BR})[\varepsilon_m L_1 + \varepsilon_d(1-L_1)] + Q(\varepsilon_m - \varepsilon_d)[\varepsilon_d(1-L_2) + \varepsilon_{BR} L_2]}{[\varepsilon_d L_2 + \varepsilon_{BR}(1-L_2)][\varepsilon_m L_1 + \varepsilon_d(1-L_1)] + Q(\varepsilon_m - \varepsilon_d)(\varepsilon_d - \varepsilon_{BR}) L_2(1-L_2)} \right\} \qquad (2)$$

where ε_m, ε_d, ε_h, and ε_{BR} are the dielectric functions of the metal bulk, the adsorbed molecules, the substrate, and the effective function of the medium, respectively [88].

SEIRAS method has been mainly used for analysing coinage metals and platinum metals, but it was shown that this method could be used also for other metals like Bi [87,89], Sn [85] and Cd [90]. Within ILs, the surface enhancement has been previously shown for Au and Pt [60,91–93], also showing how the potential dependant restructuring of the EDL in some ILs is kinetically hindered due to anion conformations. Fig. 3 shows the neat IR spectrum of $EMImBF_4$ IL and table 2 summerizes the major IR absorption peak positions of the spectrum.

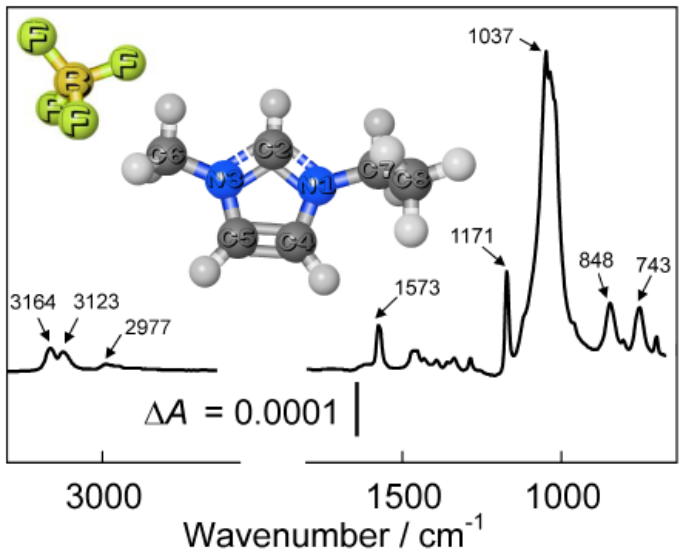

Figure 3. IR spectrum of neat $EMImBF_4$ IL calculated for monolayer absorbence. Numbering of some atoms in $EMIm^+$ cation used for infrared peak assignment.

Table 2. $EMImBF_4$ ATR spectrum interpretation.

Wavenumber / cm^{-1}	Vibration type	Vibration characterization
3164	ν	Symmetric C2-H; C4-H; C5-H stretching
3124	ν	Asymmetric C2-H; C4-H; C5-H stretching
1573	ν	Asymmetric C2; N1 stretching
1171	δ	C2H in-plane rocking
1037	ν	B-F stretching
848	δ	C2-H out-of-plane rocking
756	δ	C4-H; C5-H out-of-plane rocking
704	δ	C2-H; C4-H out-of-plane twisting

ν – valence band, δ – deformation band

4.4. Cyclic voltammetry

Cyclic voltammetry is widely used as the first electrochemistry experiment to acquire qualitative and quantitative information about electrochemical systems. In the CV method, the electrode potential, *E*, is cycled with a constant scan rate,

$v = dE/dt$, between two potential extrema (the applied potential varies linearly), and the current value is recorded. The resulting current *vs*. potential plot, the cyclic voltammogram, gives an overview of the processes occurring at the electrochemical interface [94–96].

For a simple fully reversible redox reaction, it is possible to express the development of the current density at the electrode as (at 25°C):

$$j = n\mathrm{F}D\left(\frac{\partial c_{red}}{\partial x}\right)_{x=0} \tag{3}$$

where j is current density, n is number of electrons, F is Faraday constant, D is diffusion coefficient, $\delta c_{red}/\delta x$ is the concentration gradient of reduced species. For a reversible one electron transfer reaction ($n = 1$) when $D_{\mathrm{ox}} = D_{\mathrm{red}}$ (ox – oxidized form, red – reduced form), the difference between oxidation and reduction current peaks is 58 mV [94,96].

Usually electrode potential is scanned linearly to the negative potential extreme first (forward scan) and thereafter in reverse (backward scan) to the positive potential extreme, and back to the initial potential value. If there are charge transfer processes taking place within the measured potential range, current peaks, corresponding to reduction (forward scan) or oxidtation (backward scan) processes, will emerge. The peak current, j_{p}, is described by the Randles-Sevcik equation for fully reversible systems:

$$j_p = (2.69 \cdot 10^5)\, {n_{mol}}^{3/2}\, Sc\, D^{1/2}\, v^{1/2} \tag{4}$$

where n_{mol} is the number of moles of electrons transferred in the reaction, S is the area of the electrode, c is the analyte concentration, D is the diffusion coefficient, and v is the applied potential scan rate [94,97].

One can distinguish three major groups of electrode processes; charge-transfer controlled reactions, electrode adsorption controlled processes and mass-transfer limited processes. In case of the adsorption step limited process the current peak value is proportional to the potential sweep rate applied. Furthermore, the charge circulated during the sweeps can provide information on the surface coverage of adsorbed species. For diffusional mass-transfer step controlled processes, the peak current is directly proportional to the square root of the potential scan rate. Charge-transfer limited processes can exibit highly complex kinetic behaviour [94,96–98].

The exact shape and quantitative features of the voltammograms depend on a variety of parameters, for example the adsorption isotherm followed, the surface concentration of the redox species, the presence or absence of intermolecular forces between the adsorbed molecules and reversibility of electrochemical reactions [94,96].

4.5. Electrochemical impedance spectroscopy

Impedance spectroscopy and alternating current impedance method have grown in popularity in recent years. Initially applied for the determination of the EDL capacitance and in AC polarography, nowadays are often applied to characterise processes at complex interfaces. Electrochemical impedance spectroscopy (EIS) studies the system response to the application of a periodic small amplitude AC voltage signal by measuring the current through the electrochemical cell. Analysis of the system response contains information about the interface, its structure and reactions taking place at the interface [99,100].

During the experiment sinusoidal perturbations are applied to the electrochemical system:

$$E(t) = E_A \sin \omega t, \tag{5}$$

where $E(t)$ is the potential at time t, E_A is the potential amplitude, ω is the angular frequency with a relationship to frequency f in Hz: $\omega = 2\pi f$. The current response $I(t)$ will be a sinusoid at the same frequency but shifted in phase in case of capacitive or inductive interfaces:

$$I(t) = I_A \sin(\omega t + \Phi), \tag{6}$$

where $I(t)$ is the current at time t, I_A is the current amplitude and Φ is phase angle shift by which the voltage follows the current. According to the Ohm's law, the impedance is defined as the ratio of voltage and current

$$Z = \frac{E(t)}{I(t)}. \tag{7}$$

Impedance has magnitude and phase angle and thus is a vector quantity. Therefore, it is convenient to be presented as

$$Z = Z_A(\cos \Phi + i \sin \Phi) = Z' + iZ'', \tag{8}$$

where $i = \sqrt{-1}$, Z' is real part of impedance, and Z'' the imaginary part of the impedance [100–102].

The EIS method is destructive in principle, meaning that a small AC voltage signal is applied to the interface which induces a counteracting AC current to stabilize the interface. By applying signals of differing frequencies, processes taking place with different time constants can be probed. In general, for electrochemical systems, three main non-distributed fundamental processes that can be ascribed are: resistive (such as faradic charge transfer) corresponding to a 0-degree phase shift between the voltage and current signals; diffusion (such as semi-finite length diffusion of reactants) corresponding to a −45-degree

phase shift, and capacitive (such as purely electrostatic, adsorption rate limited electrical double layer formation with capacitance) processes that show a −90-degree shift between the AC voltage and current signals. The dependence of the interfacial resistance on applied signal frequency can be calculated from the measurement and plotted in a complex plane whereby the real part of the resistance Z' (ω) shows the resistive and the imaginary part Z'' (ω) shows the capacitive part of the interfacial resistance. Calculated complex resistance plots based on certain electrical equivalent circuit (EC) elements can be fitted to the experimental data, with each component representing one physical process that takes place at the electrochemical interface. Dependent upon the measurement quality, each set of data can be described by one or more ECs and the quality of the fit can then be evaluated based on statistical fitting error. Each possible physical process ascribed to an interface can be represented as a separate element (or combination of elements for diffusion) in the overall equivalent scheme and its validity can be tested based on its effect on the overall fitting error. If the addition of a free variable does not decrease the overall fitting error by at least 50%, it is considered to not be a descriptive part of the overall equivalent scheme that characterizes the interfacial processes [103]. By ascribing all the possible physical processes that can occur at the interface and testing their validity, one can derive an overall equivalent scheme that best fits the measurement results and thus the occurring interfacial processes.

5. EXPERIMENTAL

5.1. Electrode fabrication and characterization

Pb, Au, Bi and amorphous carbon (aC) thin-layer films were deposited using AJA International UHV magnetron sputtering system applying the following parameters: base vacuum 10^{-9} Torr, 3 mTorr Ar pressure. The film deposition rate was controlled using a quartz crystal microbalance. Atomic force microscopy (AFM) images were measured by Agilent Technologies Series 5500 system in either non-contact or contact regime. Table 3 outlines the major technical parameters for thin film deposition [55,56,104].

Table 3. Technical parameters for magnetron sputtering.

Deposited electrode	Power source	Deposition rate/ Å s^{-1}	Temperature/ °C	Target purity
20 nm aC	200 W DC	0.2	190	99.999% graphite
20 nm Bi	25 W RF	1	25	99.999% Bi
20 nm Au	10 W RF	0.1	100	99.999% Au
50 nm Pb	25 W RF	1	25	99.995% Pb

Graphene electrodes were prepared from chemical vapor deposition grown single layer graphene films on copper foil (from Graphenea), which were attached onto glass plates using an epoxy glue, followed by dissolution of the Cu layer with 1 M $FeCl_3$ solution during 40 min at 60°C. 10 μm thick HOPG films were ripped from a HOPG cube (Veeco) [71]. The crystallographic orientation of the Bi(*hkl*) single crystals was determined and controlled by the X-ray diffraction method [105].

5.2. Infrared spectroelectrochemistry measurements

The IR spectroscopic measurements were performed using a PerkinElmer Spectrum GX FTIR equipped with a liquid nitrogen-cooled mid-range MCT detector and the electrochemical measurements were conducted using an Autolab PGSTAT 30 potentiostat in a three-electrode glass cell (Fig. 2) with an Ag│AgCl wire in the same IL as a quasi-reference electrode. $EMImBF_4$ from Sigma-Aldrich (>99 %, "for electrochemistry", H_2O ~150 ppm) or Solvionic (99.5 %, H_2O ~100 ppm) was additionally dried in ultrahigh vacuum at 90°C for 24 h, until reaching a pressure of $5 \cdot 10^{-9}$ Torr and water content below the detection limit of Karl-Fischer method (< 10 ppm) [55,56,104].

A thin (~5 μm) HOPG layer is glued onto the ZnSe hemisphere with a thin layer (~300 nm) of dielectric epoxy glue and exfoliated with scotch tape. Usually only one exfoliation is required to produce a see-trough layer of thin-film graphite on the hemisphere. Although the produced surface is somewhat uneven, the hemisphere setup requires only the middle, infrared active part of the hemisphere to be uniformly covered. Optical transmission and Raman spectroscopy measurements suggest the thinner parts of the electrode to compose of <10 layers of graphene. Fig. 4a shows the experimental setup of the thin film measurements [106].

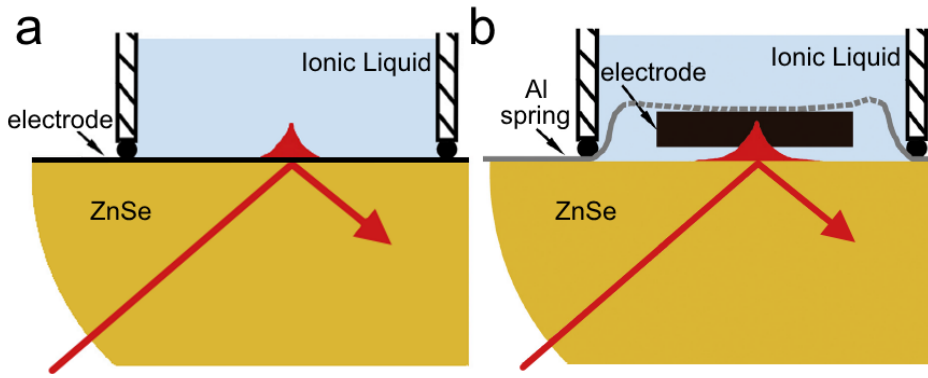

Figure 4. Infrared setup configuration for IR measurements with Pb, Au, Bi, graphite (a) and CDC(TiC) electrodes (b).

The carbide-derived carbon (CDC) porous supercapacitor electrodes were prepared from 0.2-2 micrometre sized carbon powder (made from TiC by chlorination process [107]) + 5% PTFE binder, roll-pressed to form a 100 μm thick electrode and sputter-coated with 2 μm thick Al layer in order to increase electronic conductivity. Aluminium contact layer is stable in dry $EMImBF_4$ due to the low solubility of formed Al_2O_3 and AlF_3 layers. The specific surface area for microporous carbon S_{BET} = 1860 $m^2\ g^{-1}$ was estimated according to the Brunauer–Emmett–Teller (BET) theory [108]. 3 mm diameter CDC(TiC) (Al layer facing upwards) electrodes were pressed against ATR hemisphere using perforated aluminium foil as a spring and an electrical contact (Fig. 5b). IL immersed between the ZnSe and the electrode from the sides as the glass cell has 6 mm inner diameter.

The choice of infrared transparent window is crucial as it gives the optical enhancement, but it also must be chemically resistant to the ionic liquid as well as to the products formed during electrolysis. Ge, Si and ZnSe materials were tested and it was found that the first two dissolve at about E > 0.2 V, which makes these materials unsuitable for the detection of anodic products. Our constructed experimental system [55,56] uses 10 mm diameter infrared transparent ZnSe (infrared refractive index n = 2.4) hemisphere as the support for the

working electrode (Fig. 4a). The small glass cell also includes a Pt spiral counter electrode and a Luggin capillary for the connection of the reference electrode to the cell. 0.4 cm^3 $EMImBF_4$ was added into the dried cell inside an argon filled glove box, and the cell was thereafter sealed with PTFE stoppers. An IR beam was directed through a ZnSe wire grid polarizer (Pike Technologies) and a ZnSe lens to the ATR hemisphere at 45 to 65 degrees of incidence. IR measurements were carried out in an inert atmosphere at the temperature of 23°C [56].

About 20% decrease in IR light energy (reaching to the detector) can be detected by placing the CDC(TiC) electrode against ZnSe surface – indicating that IR light surely reaches the electrodes and a portion of IR light is absorbed in the carbon matrix. From the intensity of IL peaks, thickness of about 1 μm can be estimated for the IL layer between CDC(TiC) and ZnSe.

The measurement setup consisted of an Autolab system as electrode potential controller and a Spectrum GX, which measures infrared spectra. 128 scans at a resolution of 4 cm^{-1} were collected at each potential and the measurement cycle was repeated at least 3 times. The resulting spectra were calculated by dividing the sample with the reference spectrum and presented as absorbance A, so that positive-going bands represent a gain of a particular species at the sample potential relative to that at the reference potential, chosen as the pzc. The measured bands were assigned to certain vibrations with the help of DFT-B3LYP calculations applying GAUSSIAN 09 software [109]. Calculated IR band frequencies were multiplied by 0.96, which is a common practice as the DFT calculation tends to overestimate the peak wavenumbers [56,104].

5.3. Electrochemistry measurements

Electrochemical measurements with graphene, aC and HOPG electrodes were conducted in a three electrode glass cell, which holds 0.35 mL of IL and also includes a Pt spiral counter electrode [56]. An Ag | AgCl wire in the same IL was used as a reference electrode and it was connected to the cell with a Luggin capillary. The cell was pressed against an electrode using a silicon seal. It is important to note that the measurements were carried out in an argon filled glove-box and before experiments the 1-butyl-1-methylpyrrolidinium dicyanamide (BMPyrrDCA) (Solvionic; purity 99.5%) was additionally dried in UHV at 110°C for 24 h, until reaching a pressure of $5 \cdot 10^{-9}$ Torr and water content below the detection limit of Karl-Fischer method (<10 ppm) [71].

1-Propyl-3-methylimidazolium iodide (PMImI), Merck, (Solapur, 99.9%, $H_2O \leq 300$ ppm) has been used for the single-crystal electrochemistry experiments. All measurements were carried out in a three-electrode electrochemical cell at a constant temperature of 23 °C. Electrochemically polished Bi(*hkl*) single crystal electrodes were used as the working electrodes, Pt net as the counter electrode, and Pt wire as the reference electrode. The reference

electrode was separated from the working electrode compartment by a Luggin capillary.

Calibration of the reference electrode potential was conducted by potentiometry measurements in a three-electrode electrochemical cell. A platinum wire immersed into a solution of $EMImBF_4$ containing the minimum quantitative amount (2.5 mM) of ferrocene (Fc) (Sigma-Aldrich, >98%) was used as the working electrode, and a platinum wire as the reference electrode. The IL was used in the reference electrode compartment separated from the $EMImBF_4$ + ferrocene solution by a Luggin capillary, which restricted the mechanical mixing of the ionic liquid + ferrocene with reference electrode IL used. A platinum net was used as the counter electrode. Thus, the overall electrochemical system for calibration of the Pt electrode was:

$$\text{Pt} \mid \text{IL} \parallel \text{EMImBF}_4\ (\text{Fc})\ (c = 2.5\ \text{mM}) \mid \text{Pt}$$

The cyclic voltammetry and electrochemical impedance spectroscopy methods were used to investigate the electrochemical characteristics of the Bi(*hkl*) | PMImI system using Autolab PGSTAT 320 with FRA II. Stable current density values were established after 3 h polarization of Bi(*hkl*) under negative potential at −1.8 V vs. Pt in the same IL. All measurements were carried out inside a glove box (MBraun, $H_2O < 1$ ppm, $O_2 < 1$ ppm).

Potential cycling rates between 1 and 100mV s^{-1} were applied and impedance spectra were measured within ac frequency range from 10^{-1} to 10^4 Hz with 15 mV ac modulation amplitude. Calculated impedance spectra, based on various ECs, have been fitted to the experimental spectra using the nonlinear least-squares minimization method. Fitting error of $\chi^2 < 10^{-3}$ has been established for all the fitted systems [105].

6. RESULTS AND DISCUSSION

6.1. (I-V) Electrochemical and *in situ* IR measurements of electrode materials

6.1.1. Analysis of AFM data

Fig. 5 shows the AFM topography images of four of the thin-film electrodes that were used in *in situ* IR experiments. It is seen that while Pb and Au electrodes (Fig. 5 b, c) look mostly similar, differing mostly in particle size, the Bi and graphite electrodes have significantly different surface structures.

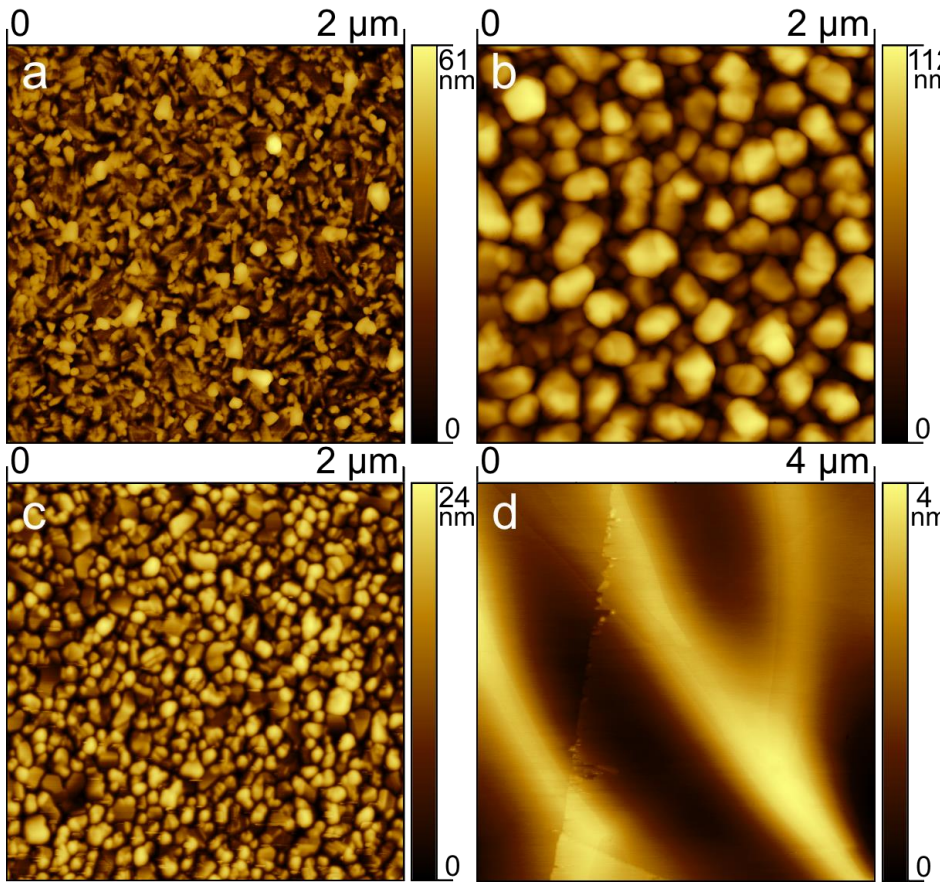

Figure 5. AFM topography images of magnetron sputtered Bi (20 nm) (a), Pb (50 nm) (b) and Au (20 nm mass thickness) (c) thin films on a glass slide and thin-film graphite electrode (d) on epoxy/ZnSe.

This is primarily because both Au and Pb are fcc metals while both Bi and graphite have a layered crystal structure. The peculiar, sharpened surface structure of Bi (Fig. 5a) is supported by the fact that XRD measurements show the thin film mostly having the Bi(111) plane exposed. The surface of the thin-film graphite electrode (Fig. 6d) is seen to have a wavy underlayer covered by large plateaus of graphite. The average plateau size is over 4 μm. Statistical parameters for the AFM images in Fig. 6 are given in table 4.

Table 4. AFM surface parameters for the surfaces described in Fig. 5.

Electrode	R	rms	Grain-size
20 nm Bi	1.043	4.2 nm	62 nm
50 nm Pb	1.205	19.1 nm	117 nm
20 nm Au	1.028	3.2 nm	72 nm
Thin-film graphite	1.000	0.7 nm	-

It is seen that while three of the electrodes are relatively smooth (R< 1.05), the Pb film has significantly higher roughness parameters, mostly due to the higher thickness of the deposited layer. That said, the grain size does not vary too much between the metallic electrodes, while no grains are seen for the graphite electrode. It should be noted that both the Pb and Au thin films are non-conductive due to being composed of spatially separate nano-islands and thus require a conductive underlayer for the measurement.

6.1.2. Analysis of CV and EIS data

Cyclic voltammetry curves in Fig. 6 [V] show that the Bi | $EMImBF_4$ system is ideally polarisable within electrode potential region from −2.1 to −0.1 V (Fc/Fc^+ in same IL) [55], while surface oxidation (dissolution of Bi) starts at 0 V, followed by redeposition at –1.4 V, as seen by the reduction peak on Fig. 6. The ideal polarizability region has been established for other metals in $EMImBF_4$ ionic liquid as well: $-1.9 < E < -0.3$ V for Pb [110], $-1.9 < E < +1.7$ V for Au. It should be noted that for all metallic electrodes, residual faradic peaks owing to the decomposition of trace water impurities are still detected at $E < -1.6$ V. For C(0001) and C(TiC) electrodes a wide region of ideal polarizability has been observed [56]. *In situ* IR data confirm that within given E region all electrodes did not show quick surface reactions [55,56,106,110].

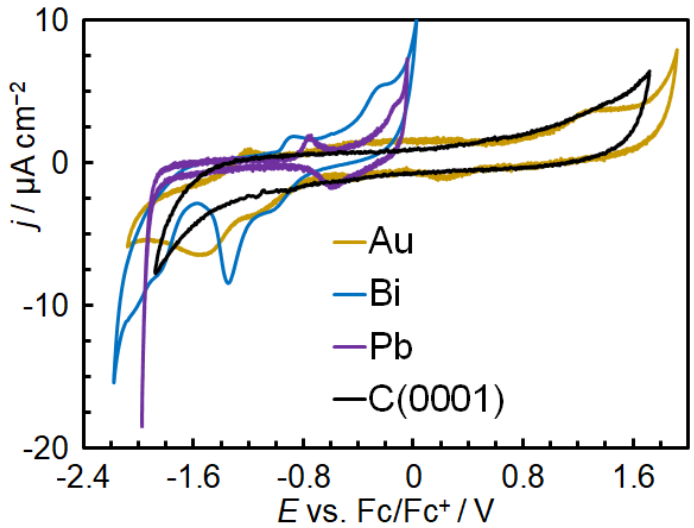

Figure 6. Cyclic voltammograms of the $EMImBF_4$ | X system measured at 10 mV/s within the region of ideal polarizability (electrochemical stability range) where X denotes the electrode material, denoted in the figure.

Series capacitance C_S values at fixed frequencies have been calculated from impedance spectra and are given in Fig. 7. The capacitance has been normalized to the R_{AFM} surface area for better comparison [15,111]. For all electrodes a clear capacitance minimum (C_{min}) has been observed with the value of E_{min} strongly dependent on the electrode material chemical composition. The C_{min} value increases in the order: C(0001) < Bi ~ Pb < Au (negative E region). Very low C_S value for C(0001) can be simulated using combined density functional theory (electrode surface layer) and molecular dynamic (RTIL layer) model, where the so-called quantum chemical capacitance [16,35,112] of the thin surface film for graphene and C(0001) plays very important role. Similarly to aqueous medium, the potential drop within C(0001) and Bi surface layers is more important than within IL layers [15,16,35,111]. It should be stressed that for C(0001) the electrical double layer region is from −1.9 to +1.7 V and at $-1.9 > E > +1.7$ reduction of cations and oxidation of anions and/or the electrode started [56].

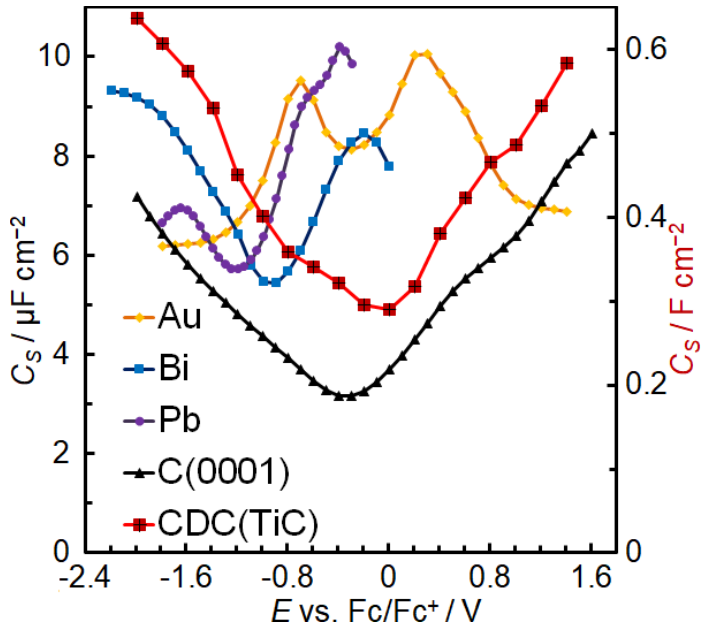

Figure 7. Capacitance vs. potential curves of the $EMImBF_4$ | X system measured at 200 Hz within the region of ideal polarizability (electrochemical stability range), where X denotes the electrode material. CDC(TiC) supercapacitor electrode areal capacitance measured at 2 mHz (right-hand axis).

For titanium carbide derived carbon CDC(TiC) very deep capacitance minimum has been observed (Fig. 7) with $E_{min} = E_{\sigma=0} = 0$ V (vs. Fc/Fc^+ in $EMImBF_4$) indicating that in addition to C(0001) (so called graphitic areas) noticeable amount of high index planes are exposed having more positive $E_{\sigma=0}$ than $E_{\sigma=0}$ for C(0001). Thus, the capacitance vs. potential data depend on the structure of the carbon electrode used. For C(0001) a very deep capacitance minimum has been measured with $E_{min} = E_{\sigma=0} = -0.3$ V (vs. Fc/Fc^+ in $EMImBF_4$).

There was only weak hysteresis in C, E curve within E −1.9 to +1.7 V. For C(0001), CDC(TiC) and semimetallic Bi C, E curves have U-shape, but for metallic Au and Pb electrodes the M-shape (so-called double maxima camel shape) C, E curves were measured. There is no significant capacitance hysteresis for Bi and Pb electrodes if the electrode potential has been cycled within the region of ideal polarizability. However, for Au there is noticeable capacitance hysteresis even when E has been kept within the ideal polarizability region. This effect can be explained by slow adsorption/desorption kinetics (formation of strongly adsorbed anions layer) at Au surface similarly to the data by Pajkossy et al. for Au(*hkl*) [19,113]. In addition, surface restructuring of Au is possible with potential cycling back to $E \approx E_{min}$.

Thus, for Au and Pb the M-shape (so-called camel shape) C, E curve, suggested by Kornyshev et al. [16,35,112], has been measured. Only for C(0001), CDC(TiC) and Bi (at $Q < 0$) there is no overcharging (if electrode kept

within electrical double layer region) effects at high negative or high positive electrode potentials (surface charge densities). Interestingly for Pb a strongly asymmetric *C*, *E* curve has been shown, similarly to H_2O + NaF (KF) electrolytes [15], indicating that BF_4^- anions have some specific interactions with Pb surface. As the image plane position depends on the surface charge density, the *C, E* curves in Fig. 7 have been integrated with respect to potential and values of ±10 and 13 μC cm^{-2} have been calculated for the C(0001) and Au electrodes, respectively. For Bi and Pb asymmetric limits of +7;−10 and +7;−4 μC cm^{-2} have been calculated. Thus, there is no large difference in the image plane position for the C(0001) electrode in comparison to the metallic electrodes based on surface charge density alone.

It should be noted that detailed fitting of C_{tot}, *E* curves to Kornyshev et al. model [16] is not very straightforward, because the surface roughness and energetic inhomogeneity effects have very pronounced influence on the C_{tot}, *E* shape, especially within $E \approx E_{min} \approx E_{\sigma\approx0}$ region [15,111]. Thus, further developments of model [35] taking into account the surface roughness and strong energetic inhomogeneity of polycristalline surfaces are inevitable for detailed analysis of capacitance, potential data. A recent article comparing three single crystal Bi planes in an IL [105] has shown that there are indeed differences in both the shape and value of *C, E* curves for the same metal but different single crystal planes, and this difference becomes very large when the specific adsorption of ions is considered. It should also be noted that the *C, E* curves for the semimetallic C(0001), CDC(TiC) and Bi electrodes do not inherently support the existence of "two" double layers, as neither show a capacitance decrease at extreme negative surface charge values [16,35,112]. This is likely due to interaction between the ionic and electronic part of the EDL which causes a significant shift in the interfacial ionic structuring when the centre of electronic charge is located within the electrode surface (carbon electrodes) or very close to the electrode surface (Bi).

6.1.3. Analysis of Pb│EMImBF$_4$ interface

The *in situ* SEIRA technique has successfully been extended for the study of thin film Pb electrodes [IV]. Fig. 8 shows the potential dependent p-polarized SEIRA spectra for the 50 nm thick Pb layer deposited onto a silicon hemisphere, measured relative to the pzc. The s-polarized spectra show the exact same intensities and dependences in this system. The spectral region between 1140 and 1080 cm^{-1} shows typical noise caused by the absorption of the Si substrate and were removed from Fig. 8. The produced spectra are seen to have relatively narrow peaks, in accordance with other SEIRA measurements [86] and are interpreted to stem from the first surface layer alone, i.e. the dense layer, with the changes in the spectra governed by the surface selection rule [81]. Thus, positive peaks in the spectra result from either the dynamic dipole of a particular species turning into a position more perpendicular to the surface relative to that of the pzc or an increase of a particular species at the surface, relative to the pzc. The two different modes can be distinguished between by

looking at the whole spectra of a particular species (either anion or cation); if all changes are in the same direction, a change in surface coverage is likely the cause, while changes in orientation produce peaks in both directions. It is to be pointed out that only peaks within the 1060 to 980 cm^{-1} spectral region are produced by the anion and thus it is difficult to assess changes in anion orientation due to the symmetrical shape of the species. From literature [114] it is known that a 'free' (this is interpreted as a solvated tetrafluoroborate anion with specific interactions with the solvent alone) tetrafluoroborate anion is expected to have a triply degenerate asymmetric stretching vibration at 1100 cm^{-1} and a solvated contact ion pair with lithium cation would have an infrared absorption band at 1060 cm^{-1}. However, neither of these peaks are observed for the neat IL by us [115] or others [116]. Instead, a broad peak is observed between 1060 and 1020 cm^{-1}. Interestingly, for the interface between $EMImBF_4$ and different semimetals, such as bismuth [117], amorphous carbon [115] or thin-film graphite [106], the same peak is observed at 1020 cm^{-1} or even lower wavenumber. All this suggests that the anions in the IL are not 'free' (with no specific interactions) and can instead be described as forming different associate structures (specifically interacting multi-ion associates) that could change with respect to electrochemical polarization due to stronger specific interactions of ions with the electrode surface. It can be interpreted that the changes in the position of the anion asymmetric stretching vibration are both due to ion-ion interactions as well as ion electrode surface interactions, which will be further discussed when considering the impact on the EDL formation.

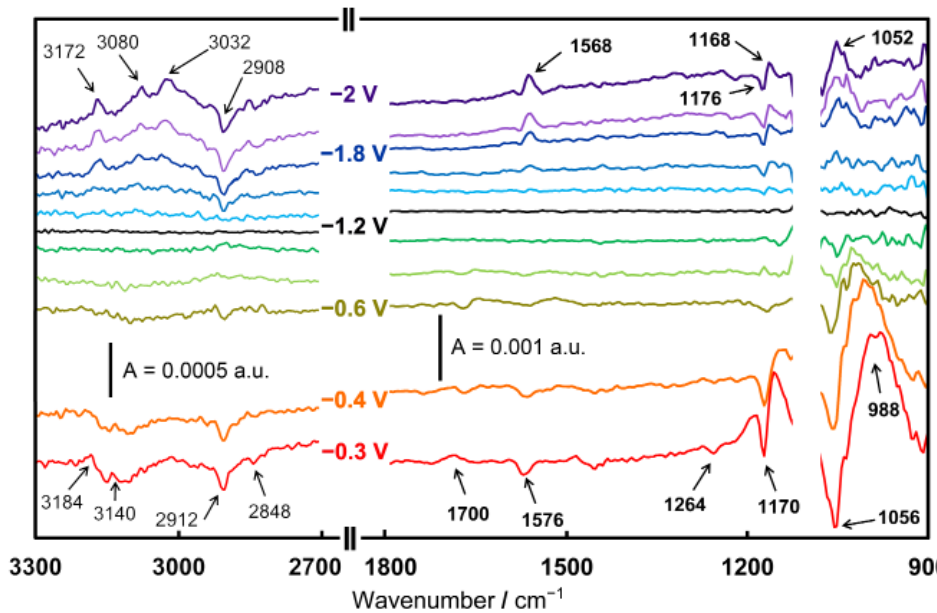

Figure 8. P-polarized *in situ* SEIRA spectra for 50 nm Pb on Si │$EMImBF_4$ system at selected potentials within the electrochemical stability limits. Electrode potential of −1.2 V was used as the reference potential and is shown for clarity.

$EMIm^+$ cation peaks for the Pb | $EMImBF_4$ system are interpreted as: 3172 (νC2−H stretch), 3140 (νH−C4C5−H asymmetric stretch), 3032 (νC2−H−Pb stretch), 2908 (νC8−H symmetric stretch), 1568 (ring inner plane asymmetric stretch, νC2–N1−C4), 1168 (δC2–H inner plane rock). Numbering of atoms in $EMIm^+$ cation is shown in Fig. 3. The assignment of peaks is done with guidance from quantum chemical calculations also considering solvation. However, due to extremely strong electrostatic forces at the interface, it is difficult to model the ions at the interface as either ion pairs or separate ions, with the directions of the dynamic dipole moments between the two seen as highly significant and thus accurate accounts for the cation tilt angle are difficult if not impossible to establish. Qualitative assessments of the changes at the interface can nevertheless still be made. The cation is seen to shift from a more parallel orientation at the pzc to a perpendicular orientation at most negative potentials with the ethyl group (2912 cm^{-1}) significantly more parallel to the surface normal than at pzc. As the ethyl group rotates quite freely anyway, the negative IR peak can be also explained as it fades away from the surface at negative potentials, compared to pzc. A graphical representation of this is shown in Fig. 9.

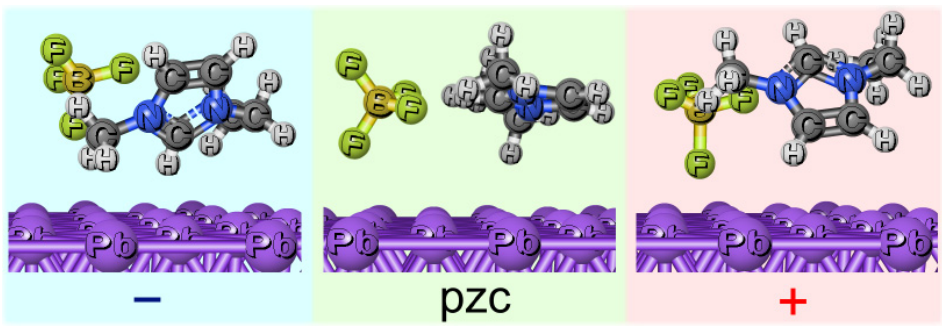

Figure 9. Graphical representation of the reorientation of ions at the Pb interface at positive (+), neutral near pzc and negative (−) polarization according to the spectra shown in Fig. 8.

The C2-H hydrogen is seen to be pointing toward the surface (new peaks at 3080, 3032 cm^{-1}) while the bipolar nature of the cation peaks at 1568 and 1168 cm^{-1} also show that the cation vibrations are less effected by interactions with anions at extreme negative potentials, as the peaks shift from ion associate like vibrations to a spectrum characteristic of separate ion vibrations. It is interesting to note the increase of the anion asymmetric stretching vibration at negative potentials, which could be explained by the weaker interaction between the anion and the Pb electrode surface at more negative potentials, allowing for more intensive vibrational states (the anion is considered to adsorb in the 1-F-down orientation, retarding the perpendicular vibration and producing weak parallel vibrations). Such treatment considers that the anion adsorption is

somewhat chemical in nature (and is in line with DFT calculations produced for Bi (111) [37]). The spectra show that both ions are at the surface or in the spectral vicinity at both extremes of the ideal polarizability potential region, as no complete ion exchange at the surface has been established.

The cation is seen to shift to a more perpendicular orientation to the surface normal at positive potentials, relative to the pzc, and shown graphically in Fig. 9. At these potentials the C2-H hydrogen is seen to point away (peaks at 3184, 3140 cm^{-1}) from the surface with the ethyl group (2908 cm^{-1}) again nearly parallel to the surface (fades away from the surface), thus producing a configuration in which the centre of cationic charge is shifted as far away from the surface as possible.

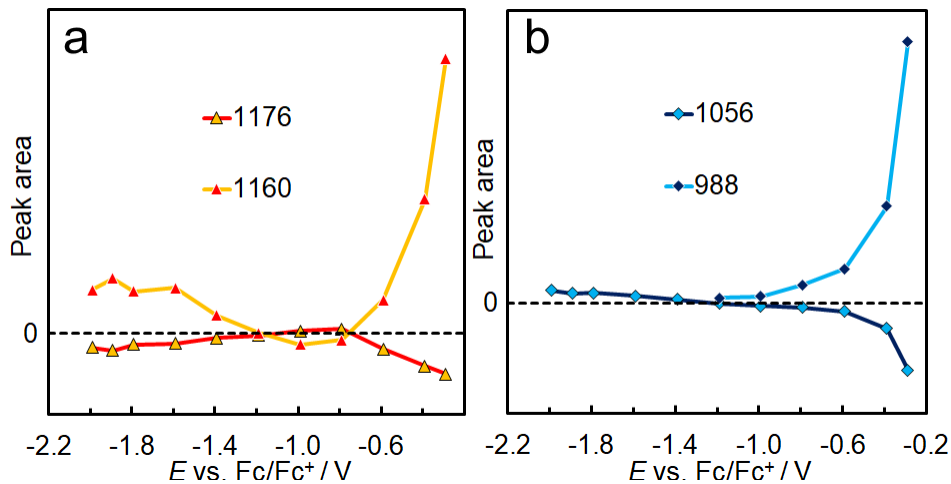

Figure 10. Integrated peak areas of the p-polarized *in situ* SEIRA spectra for 50 nm Pb on Si | EMImBF4 system. The anion (BF_4^-, peak at 1056 cm^{-1}) (a) and cation ($EMIm^+$, peak at 1170 cm^{-1}) (b) peak areas are shown relative to the pzc at −1.2 V.

Of particular interest is the strong bipolar behaviour of the anion peaks, shifting to almost 70 cm^{-1} lower wavenumber at most positive potential region. Integrated band intensities are demonstrated in Fig. 10b. Such a large change is rarely seen even for SEIRA spectra and is attributed to the complete dissociation of the ion association (ion-ion interactions) within the dense layer and a high surface coverage of anions at the Pb film electrode surface. This would signify a shift from ion-associate-like screening at potentials near the pzc (for example, dipole screening interaction) to charge based screening at the potential extremes (primarily coulombic interaction). The same effect, albeit a smaller shift (up to 16 cm^{-1}) is observed, too, for the cations at both positive and negative potential extremes, shown in Fig. 10a. Interestingly, this strong bipolar behaviour of the ion absorption peaks mainly coincides with the capacitance maxima of the *C, E*

curve, providing additional reasoning for the shape of the *C, E* curve in Fig. 7, particularly as to why a decrease of capacitance is observed at extreme potential.

The association of ions has been used as an explanation for the characteristic behaviour of ILs at metal interfaces as well, even to the extent to suggest ILs to behave as dilute electrolyte solutions [118]. However, different from that particular article, the results of our *in situ* SEIRA measurements for the Pb | EMImBF4 interface do not suggest the existence of long-lived, stable ion pairing between cations and anions, which is an important distinction to be made. A recent theoretical study [119] has shown that within a mean-field level of theory, only a third of the particles constituting an IL can be described as ion pairs, and that those pairs would be relatively short-lived. However, because the study adopts the general hard-spheres description of an IL, this result cannot be considered absolute. Indeed, when considering the spectra of a neat IL, no differentiation between ion pairs, 'free' ions or a particular ion association structure can be made. Unsurprisingly, in order to simulate infrared spectra of ILs quantum mechanics are required [116,120], confirming that ion association is indeed a significant part of the description of ILs, although describing them as a solution of ion pairs is a major oversimplification.

6.1.4. Analysis of Au | $EMImBF_4$ interface

Fig. 11 shows the p-polarized SEIRA spectra for the 20 nm Au film deposited onto a ZnSe hemisphere previously coated with 20 nm layer of aC required for electrical conductivity of the Au layer. It should be noted that identical experiments have been conducted with Si hemisphere and no aC underlayer (the Si hemisphere is in itself conductive) and almost identical spectra were measured, however, since the dissolution of Si starts at +0.2 V the positive potential limit could not be probed. Even with a passive aC [115] underlayer it was not possible to measure the whole range of positive potentials up to +1.6 V as in electrochemistry measurements because of surface oxidation of Au at $E >$ +1.2 V. This reversible process is due to the water impurities and does not significantly hinder electrochemistry measurements. For *in situ* IR, however, means that surface enhancement effect is altered and thus the background signal becomes unstable. Overall, the potential dependence of spectral features is similar for the Au | $EMImBF_4$ system as that seen for the Pb | $EMImBF_4$ system: sharp potential dependent peaks for the BF_4^- anion between 1000 and 1030 cm^{-1} and complex, mostly bipolar peaks for the $EMIm^+$ cation. The potential dependence of the most intense cation and anion peaks are shown in Fig. 12. The peak areas for the $EMIm^+$ cation have been multiplied by 15 for better comparison (15 corresponds to the spectral ratio of anion-to-cation peak area in neat $EMImBF_4$ IL). A basic bipolar dependence is observed from the peak area dependence on potential, however, it should be noted that the exchange between anions and cations is significantly more intense at potentials

more positive of the pzc than in the negative polarization range. This is likely due to the electrophilic nature of Au as well as smaller ion volume for the tetrafluoroborate anion compared to that of the imidazolium cation. It can also be observed that the decrease for the anion signal at 1016 cm^{-1} largely stops at −0.9 V and levels off thereafter. This is likely due to the extreme surface enhancement effect of the Au electrode [88], whereby the depletion of the compact layer of anions results in the system effectively becoming "blind" to the change of anion concentration in the EDL. That said, we can still observe changes as well as increase in the cation absorption spectra down to −1.9 V, consistent with the interpretation that only ions within the compact layer are probed. It should also be noted that the potential at which no more significant changes in the anion spectra are observed correlates well with the negative potential peak of the *C*, *E* curve for the Au | $EMImBF_4$ system and could relate to the formation of such a feature. The same cannot be observed in the positive polarization region as the peaks show changes up to the potential limit of +1.1 V. As far as the bipolar peak behaviour observed for the Pb | $EMImBF_4$ system is concerned, the same basic dependence is also observed in case of Au electrode, however, on a smaller scale for the anion peaks.

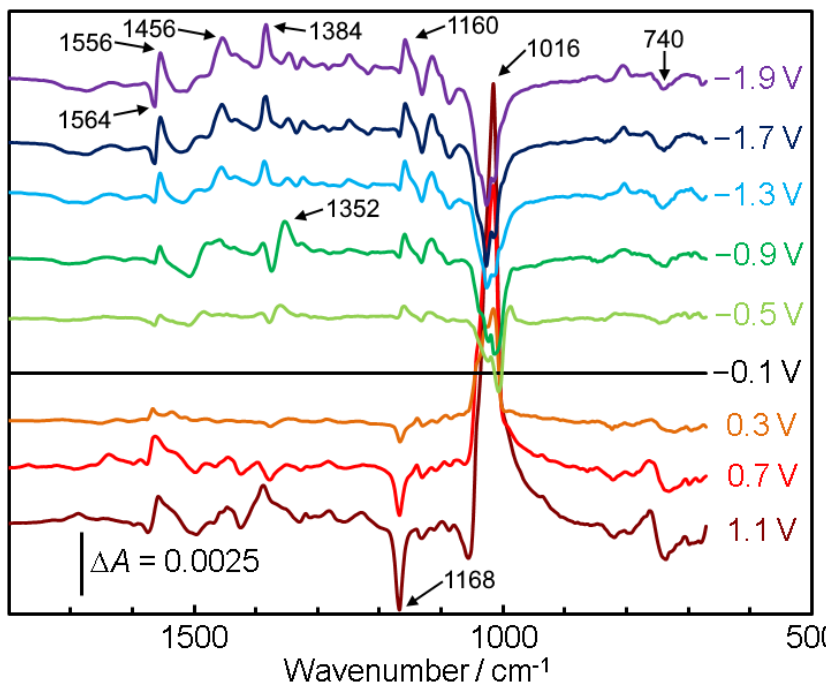

Figure 11. P-polarized *in situ* SEIRA spectra for 20 nm Au on aC/ZnSe | $EMImBF_4$ system at selected potentials within the electrochemical stability limits. Electrode potential of −0.1 V (pzc) was used as the reference potential and is shown for clarity.

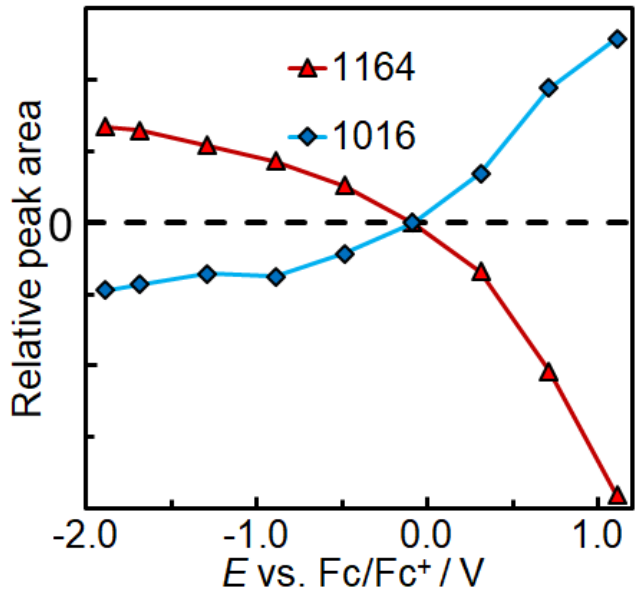

Figure 12. Comparison of the anion (BF_4^-, peak at 1016 cm^{-1}) and cation ($EMIm^+$, peak at 1164 cm^{-1}) peak areas relative to the applied potential for the *in situ* SEIRA spectra of the 20 nm Au │ $EMImBF_4$ interface measured relative to the reference spectrum at −0.1 V from the data seen in Figure 11.

It is observed that the major anion absorption peak shifts from 1032 cm^{-1} at extreme negative polarization region to 1016 cm^{-1} at most positive potential of +1.1 V. For the $EMIm^+$ cation, multiple strong bipolar peaks are observed thorough the whole wavenumber range at 1560, 1360, 1164 and 740 cm^{-1}. These peaks signify that not only the concentration of cations within the compact layer is changing but that the orientation also changes. Similar to the Pb system, the cation is seen to orient with the C2-H hydrogen toward the Au surface in the negative polarization range, resulting in strong bipolar absorption peaks at 1560 and 1164 cm^{-1}. For the positive polarization range an orientational determination is more difficult to make as complete depletion of the compact layer of cations is considered to take place. Overall, the double layer behaviour as well as spectral dependence is highly similar for both Pb and Au systems. The overall shape of the absorbence vs. potential graph is very close to that calculated based on the Oldham model [17] and considering exponential decrease of signal with distance [91], particularly in the negative polarization range.

6.1.5. Analysis of Bi│$EMImBF_4$ interface

Fig. 13 shows the potential dependent *in situ* IRA spectra of the 20 nm Bi│$EMImBF_4$ system [I]. Although the spectra show high intensity of IL band

changes, they are completely different from the spectra for Pb and Au. All the spectral bands are positive relative to the reference potential at pzc, however, the spectral absorption bands do not correspond to the neat $EMImBF_4$ IL. Both the major cation and anion bands are shifted toward lower wavenumbers and the intensity ratio of the representative bands is seen to change relative to applied potential, as shown in Fig. 14.

The peak intensities in Fig. 14 are normalized corresponding to the ratio of the neat, liquid spectrum of $EMImBF_4$ [115]. It is observed that at positive polarization the ratio increases toward higher anion peak absorption and at negative polarization the ratio increases toward higher cation peak absorption. These factors suggest that the absorption bands indeed correspond to changes within the EDL, but the spectral enhancement is completely different from that of Au and Pb [60,110]. Given that Bi has significant semi-metallic properties [117,121], this is also to be expected. Overall, the spectral results suggest that the absorption bands originate primarily from the change in the diffuse part of the EDL, where increased layering of IL-associates takes place in addition to the direct charge compensation shown by relative band intensities. This is in accordance with in situ AFM force-distance curves in IL media [122,123]. Interestingly, the IR band intensities show almost identical dependence to the *C*, *E* curves measured for the same electrode in Fig. 7.

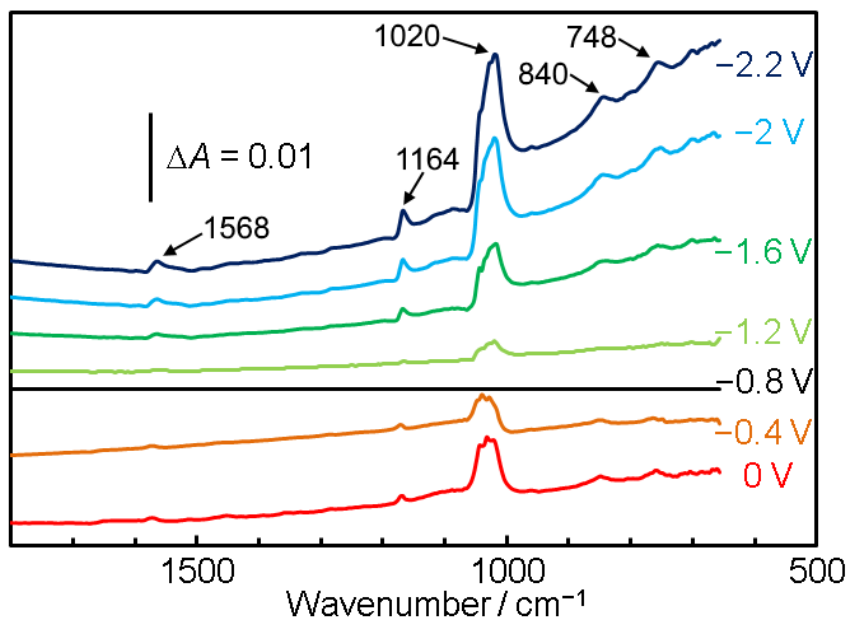

Figure 13. P-polarized *in situ* IRA spectra for 20 nm Bi on ZnSe │$EMImBF_4$ system at selected potentials within the electrochemical stability limits. Electrode potential of −0.8 V was used as the reference potential and is shown for clarity.

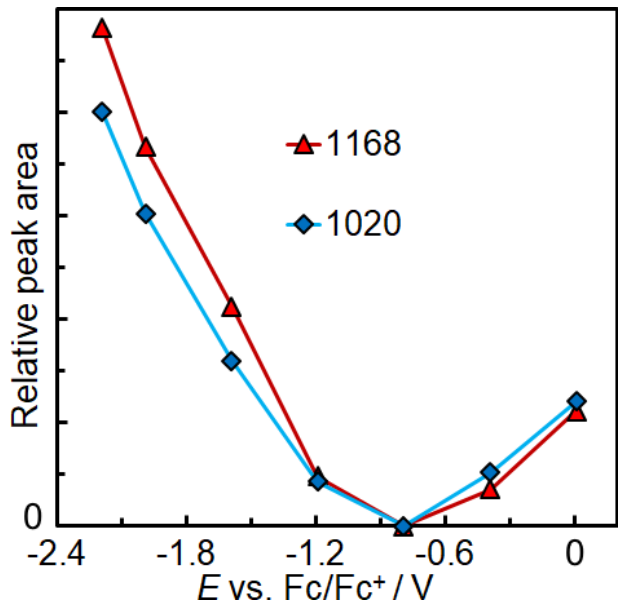

Figure 14. Comparison of the anion (BF_4^-, peak at 1020 cm^-) and cation ($EMIm^+$, peak at 1168 cm^{-1}) peak areas relative to the applied potential for the *in situ* IRA spectra of the 20 nm Bi │ $EMImBF_4$ interface measured relative to the reference spectrum at −0.8 V from the data seen in Figure 13.

6.1.6. Analysis of thin-film graphite│$EMImBF_4$ interface

Fig. 15 shows the potential dependent *in situ* IR spectra for the thin-film graphite│$EMImBF_4$ interface [III]. Three distinct areas of different spectral information have been outlined in the figure. The most striking and perhaps most interesting are the extremely wide (approximately 1000 cm^{-1} wide) gaussian shaped peaks with very strong potential-position dependence, as shown in Fig. 16.

Such features could not be characterized by conventional theory of vibrational spectroscopy and are instead interpreted to result from the potential induced change of the reflective properties of the thin-film graphite electrode; as *in situ* ER spectroscopy [124,125] data.

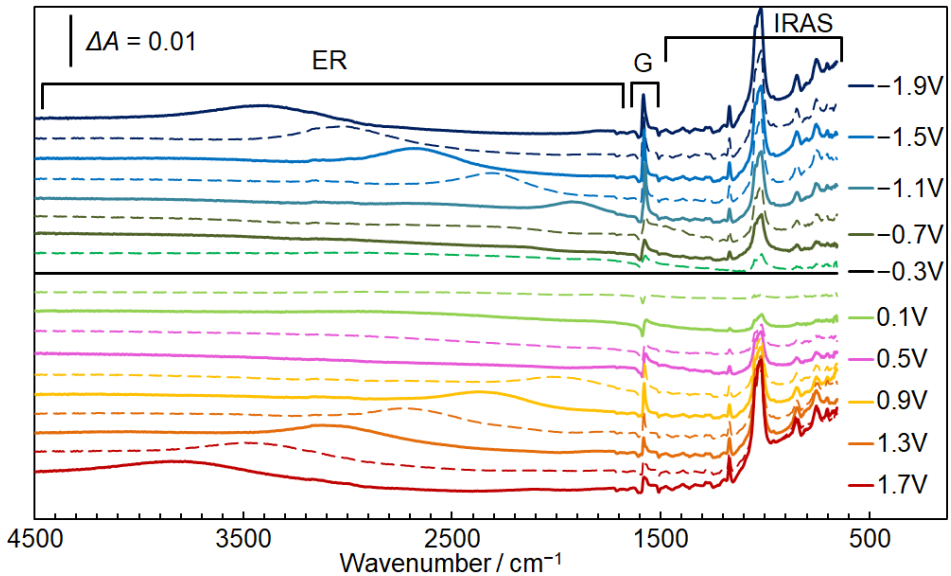

Figure 15. P-polarized *in situ* infrared spectra of the thin-film graphite on epoxy/ ZnSe | $EMImBF_4$ system. The spectra are shifted in the vertical direction for clarity. Areas where different spectral information has been extracted have been outlined.

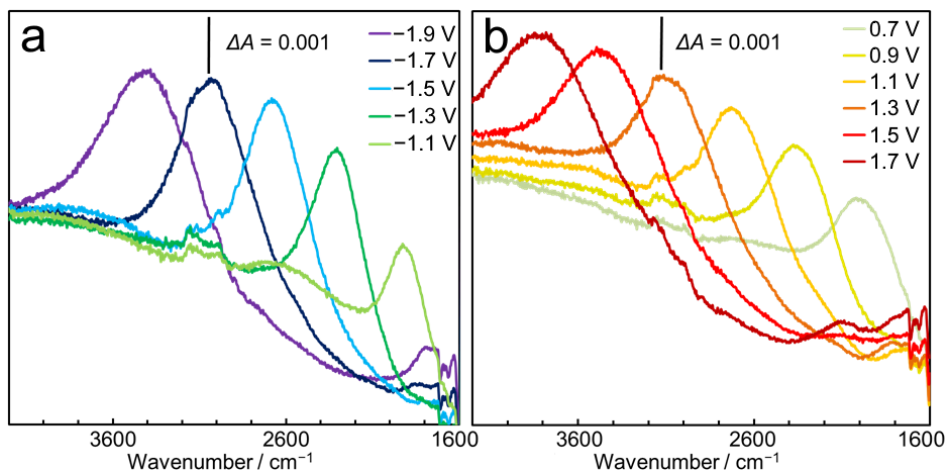

Figure 16. P-polarized *in situ* infrared spectra of the thin-film graphite | $EMImBF_4$ system outlining the electroreflectance area of Fig. 15 for negative (a) and positive (b) polarization regions.

From a fundamental standpoint, the peaks signify the excitation of electrons to the empty π-orbitals of graphite at the K point [126] by infrared irradiation, which shift due to the applied electric potential at the interface. Due to the limited spectral range and other spectral features, the peaks are either not seen

or easily detected within the range from 0.4 to −0.6 V. Fig. 17a shows the potential E dependence of the peak maxima E_{dip}.

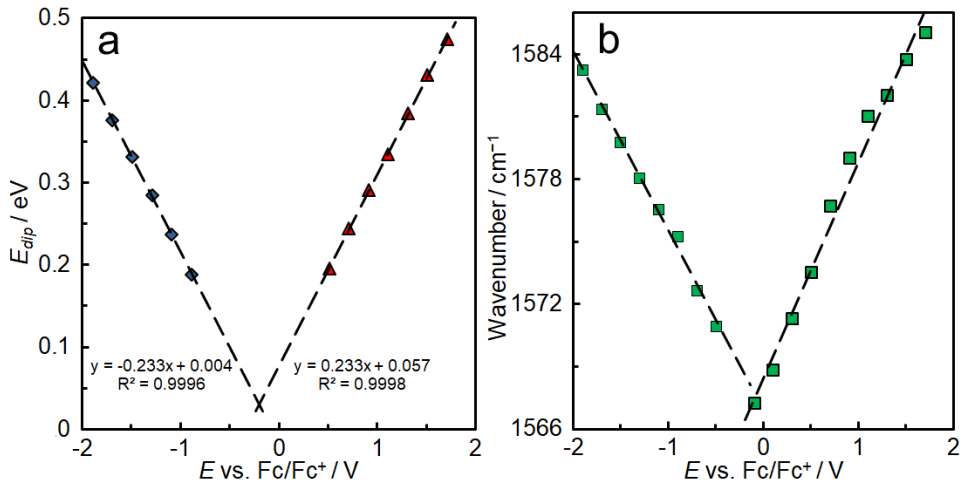

Figure 17. The dependences of E_{dip} (a) and G band position (b) on electrode potential from the spectral data in Figure 15.

It can be seen that there is an almost perfectly linear dependence between the peak dips and electrode potential, with exactly the same absolute slope of 0.233 eV V^{-1} at both the positive and negative potential side, in excellent agreement with the surface electronic structure of graphite [126]. Similar graphs of E_{dip} vs. E have been shown for low index crystal faces of Au and Ag [124,127]. However, the exact mechanism generating this effect is still under discussion. While it has been proposed that this dependency represents the applied effective field strength on the respective material surface states, such assumptions could not be confirmed by theory [124]. On the contrary, large differences exist between different crystal faces, metals and cathodic and anodic regimes for which many unconfirmed explanations have been given. More interestingly, the E_{dip} vs. E plot slopes for metal interfaces are always positive [124], contrary to what is seen in case of our measurements. Thus, it is suggested that, under the condition of ideal polarizability, the E_{dip} vs. E plot slope is specific only to the electrode surface electronic states, therefore carrying no information about the electrolyte side of the electric double layer. That said, these peaks have been confirmed [124] to offer extremely interesting information for systems with partial charge-transfer or specific adsorption and therefore ER allows conducting the electron transfer studies of graphite interfaces. Another feature in the potential dependence spectra is the G band, characteristic of sp^2 carbon materials at approximately 1570 cm^{-1}. While the ER spectra represent the shift in empty surface states, the G band is specific to the bonding between carbon atoms and thus to the filled electron orbitals. Fig. 17b shows the potential

dependence of the maxima of the G band relative to the applied electrode potential. A familiar V-shape dependence of the G band wavenumber on *E* can be seen, characteristic of the shift in electronic structure due to the applied electrode potential. Exactly the same effect has been seen in *in situ* Raman measurements of the graphene interface [128] for which the potential dependence is very similar.

Finally, the spectrum also shows the vibrational energy levels of the electrolyte side of the interface- the infrared absorption (IRA) spectra, outlined in Fig. 18.

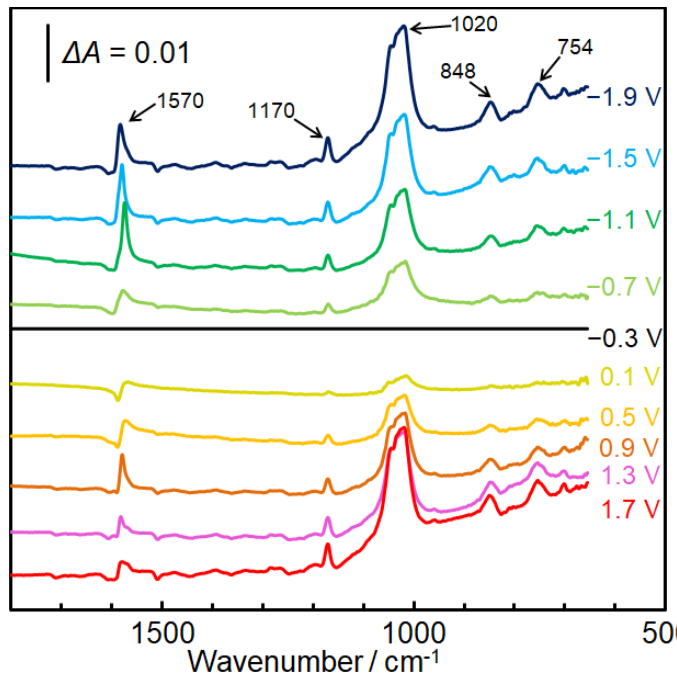

Figure 18. P-polarized *in situ* infrared spectra of the thin-film graphite | $EMImBF_4$ system outlining the IRAS area of Figure 15.

The observed peaks are interpreted to be characteristic mainly of the diffuse part of the EDL, highly similar to what was seen for the Bi | $EMImBF_4$ system. Firstly, the peak area- potential dependence with a minimum confirms the IRA spectra are very intensive, up to 50 times (200 times compared to HOPG measured in an infrared reflection-absorption setup) more so than those measured for the amorphous carbon interface [115].

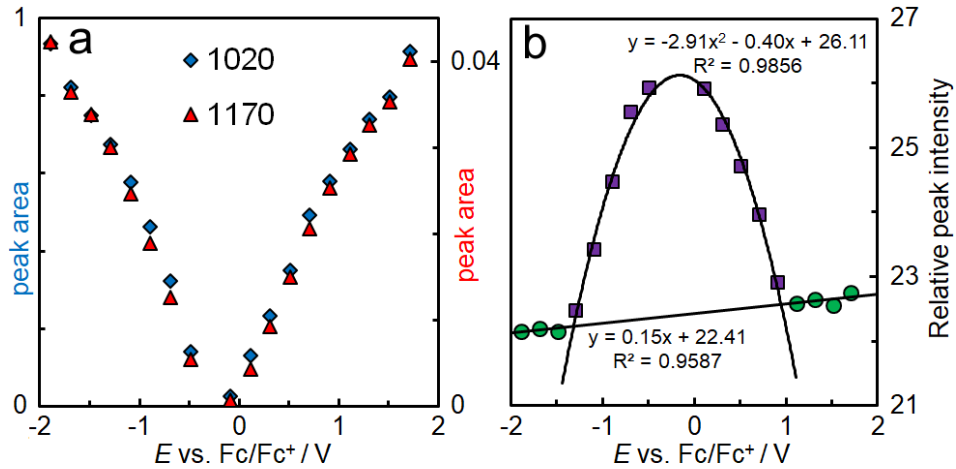

Figure 19. (a) Dependence of the major anion (BF_4^-, peak at 1020 cm^{-1}) and cation ($EMIm^+$, peak at 1170 cm^{-1}) infrared absorbance peaks on electrode potential for the thin-film graphite | $EMImBF_4$ interface. (b) Dependence of the anion-to-cation peak intensity on electrode potential from the data given in part (a).

Although the IRA spectra also represent different interfacial properties and structures as well as different electrode thicknesses (20 nm thick amorphous carbon compared to <5 nm thick thin-film graphite), such increase of signal (usually known as an enhancement effect) is rare even for rough metallic surfaces. Theoretical models [129] and experiments with graphene micro-ribbons [130] have predicted that the plasmonic resonance of graphene is applicable for spectroscopy in the terahertz frequency range. A recent article [131] has also shown that graphene nano-ribbon arrays exhibit plasmonic enhancement of adsorbed structures. Thus, it is concluded that the plasmonic resonance of graphene [132] is applicable for the investigation of the electrical double layer structure.

The V-shape of capacitance vs. potential curve has proven to originate from a semiconductor-like space-charge region inside of the electrode [12,133] highly similar to what has been shown for graphene in the same IL [134]. However, it should be noted that the overall thickness of the diffuse layer in the IL also follows this basic V-shape dependence. If we look further into the details of the compositional changes within the diffuse layer, the relative intensity of anion-to-cation peak area is shown in Fig. 19b. It should be noted that in a pristine IR spectrum of bulk $EMImBF_4$ the ratio of the most intense anion-to-cation peaks is 15 [104] so it is immediately obvious that the structure and composition at the interface is considerably altered by the screening of electrode potential. Although not quantitative, the ratio shows two general areas within the polarization region- at and near the pzc from −1.3 to +0.9 V (purple squares) we observe a parabolic dependence on potential, consistent with the consideration of the diffuse layer. It is likely that as the field strength increases

with polarization, the ion associates adopt a more favourable alignment at the interface to more effectively screen the impeding electric field [115]. Dissociation of ion associates within the diffuse layer is another probable cause [104]. It is highly unlikely that the actual ratio of anions-to-cations at the interface is the cause of this effect as the same principal response is observed for both positive and negative polarization. In the second potential area, at potentials lower than −1.3 and higher than +0.9 V (green circles), a weak linear correlation is observed at the extreme potentials, showing a decrease of the anion-to-cation ratio at the negative potential limit and an increase within the positive potential limit, consistent with direct charge compensation within the EDL, also seen for the compact layer in case of Pb and Au. Thus the results are consistent with the potential dependent layering shown by AFM and X-ray measurements as well as with the change in the degree of ion association shown by enhanced IR measurements [104,122,135].

6.1.7. Analysis of CDC(TiC)│$EMImBF_4$ interface

Fig. 20 shows the *in situ* IR spectra of the CDC(TiC)│$EMImBF_4$ interface [II] measured in the reflection-absorption configuration shown in Fig. 4b. Compared to all the previous systems, the spectra show a completely different spectral dependence: all the observed peaks are negative relative to the reference potential of −0.2 V and the absorption bands are identical to that of the neat $EMImBF_4$ IL [115]. Although it was hoped that spectra could be measured of the changes inside the porous carbon electrode, the spectral changes suggest that what is being probed is the thin IL layer directly adjacent to the porous electrode surface. Thus, the peaks form because of the actuation of the electrode caused by EDL charging, similar to what has been shown with *in situ* dilatometry measurements of similar CDC electrodes [136]. Fig. 21 shows the potential dependence of the relative peak areas of major anion and cation absorption bands based on the spectra in Fig. 20. It is observed that a negative parabolic dependence on potential is followed for both anion and cation absorption bands at 1040 and 1172 cm^{-1}, respectively.

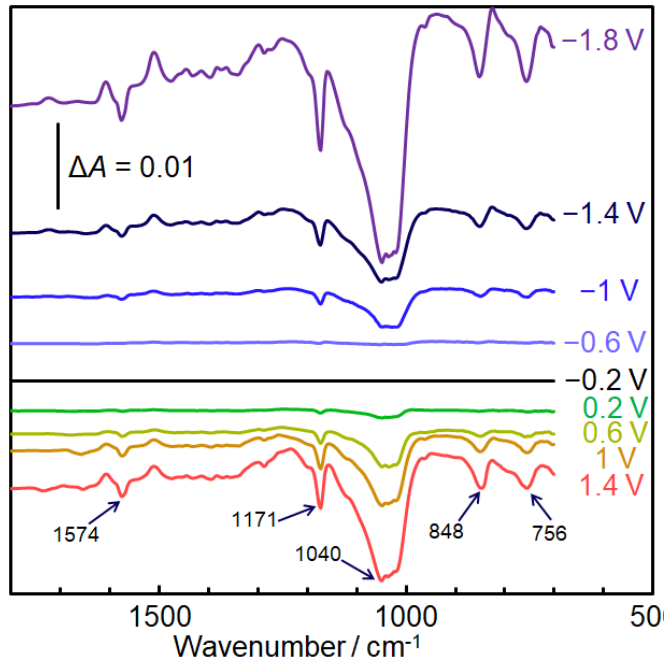

Figure 20. P-polarized *in situ* IRRAS spectra of the CDC(TiC) on ZnSe | $EMImBF_4$ interface measured relative to the reference spectrum at −0.2 V. The spectra are shifted by a constant in the vertical direction for clarity.

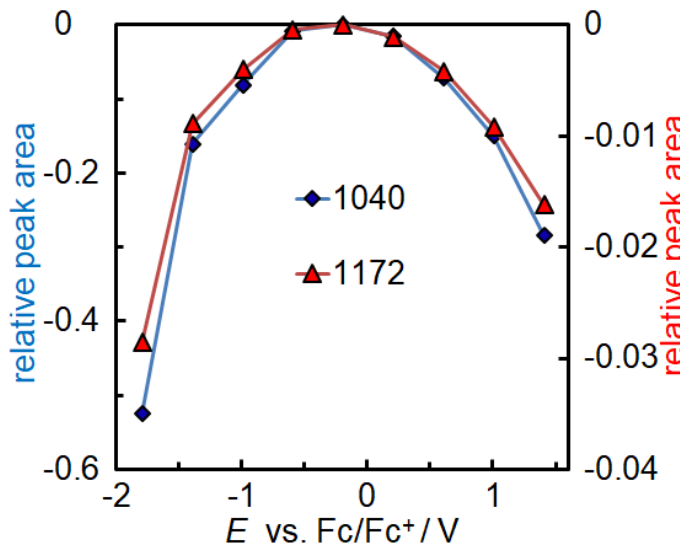

Figure 21. Comparison of the anion (BF_4^-, peak at 1040 cm^{-1}) and cation ($EMIm^+$, peak at 1172 cm^{-1}) peak areas relative to the applied potential for the *in situ* IRRAS spectra of the CDC(TiC) | $EMImBF_4$ interface measured relative to the reference spectrum at −0.2 V from the data seen in Figure 21.

The ratio of anion-to-cation peak area is between 15 and 18 for the whole polarization range, close to that of the neat $EMImBF_4$ IL [115]. This reinforces the fact that the peaks do not correspond to changes within the EDL but rather IL at the surface of the porous carbon electrode, showing that an additional amount of IL is absorbed by the CDC(TiC) electrode from the IL bulk when polarization is applied to the supercapacitor electrode [136,137]. Considering the measurements at graphite │$EMImBF_4$ interface, this is required because of the increased IL layering within the micropores of the CDC(TiC) electrode.

6.2. (VI-VII) Dielectric capacitor based on electropolymerizable dicyanamide anions

6.2.1. Analysis of CV, EIS and AFM data

CVs of the single layer graphene │BMPyrrDCA IL [VI-VII] measured up to 10 V are shown in Fig. 22. It is seen that there is a large oxidation peak at +2.2 V vs. Ag │AgCl for the first CV scan of the measurement, followed by the current levelling off at approximately half of the peak current value up to 10 V. The current value decreases close to 0 for the reverse scan at 5 V and only increases again going beyond 8 V for the second scan. After 10 CV scans the system is fully passivated up to 10 V. This kind of behaviour is not typical for IL interfaces, particularly electrode materials that do not form solid oxides and has only been show for a select few anion compositions in ILs [71,138,139]. Capacitance dependence on passivation potential is shown in Fig. 23a for three different flat carbon electrodes.

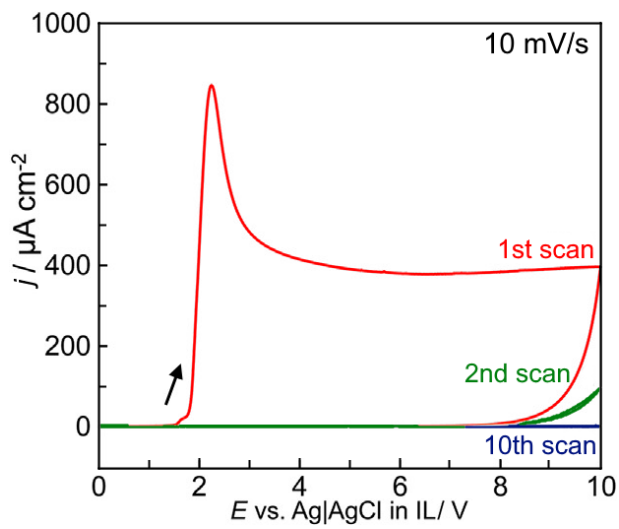

Figure 22. Passivation of single layer graphene electrode. Low scan rate cyclic voltammograms for the graphene │BMPyrrDCA system.

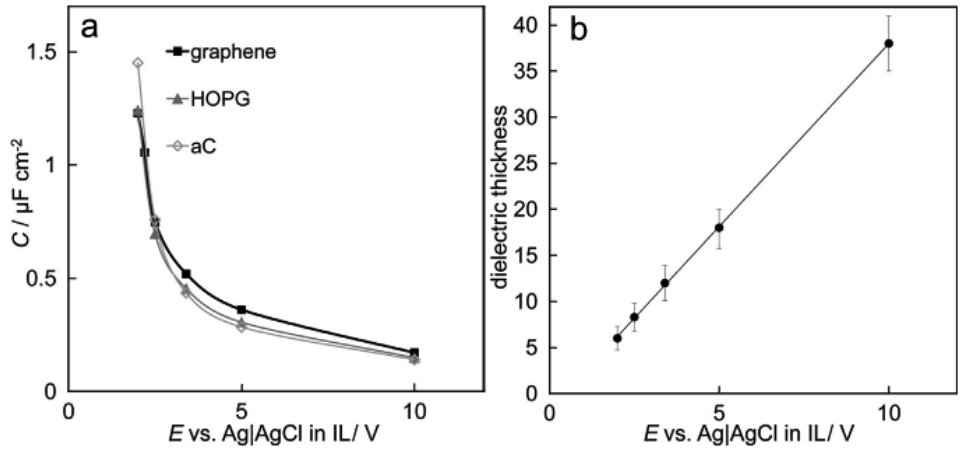

Figure 23. Dependence of capacitance (a) and dielectric thickness (b) on the passivating potential applied for the graphene, HOPG and aC flat carbon electrodes in BMPyrrDCA.

Capacitance of the passivated carbon electrodes is between 1.2 and 1.5 μF cm^{-2} at 2 V (Fig. 23a), which is nearly the same value as the unmodified graphene electrode at pzc, but 6 times lower than at −2 V [71]. It was found that the capacitance value decreases with maximal passivation potential applied; for example, at 3.4 V it is between 0.44 and 0.52 μF cm^{-2} for the carbon electrodes, decreasing down to about 0.15 μF cm^{-2} at passivation potential of 10 V. This is consistent with the consideration of a dielectric capacitor whereby the capacitance is inversely proportional to dielectric thickness.

The *ex situ* AFM data in Fig. 23b, measured for cleaned aC electrodes after passivating up to the noted potential, indicate that the film thickness after passivation up to 3.4 V is 12 nm and the thickness increases linearly with increase in passivation potential applied, up to 38 nm at 10 V. Linear increase of dielectric film thickness caused by the increase of passivation potential is an expected result; however, surprisingly high capacitance value at 2 V is a new phenomenon and could be related to the system having both properties of a dielectric- and an EDL-capacitor.

6.2.2. In situ IRA spectra of thin-film graphite│PDCA

In situ IR spectroscopy analysis performed during dielectric layer formation at aC and HOPG electrodes show a sharp absorption band at 2172 cm^{-1}, a broad absorption band in the region 1750-1050 cm^{-1} centred at 1540 cm^{-1}, and absorption bands at 766 and 718 cm^{-1}. Quantum chemical calculations indicate that =N−C≡N sequence gives an IR absorption band near 2172 cm^{-1}; thus

suggesting that the product, polydicyanamide (PDCA) has mainly a linear carbon skeleton as shown in Fig. 24.

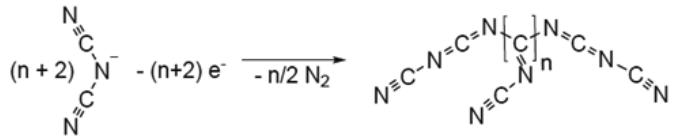

Figure 24. Proposed reaction scheme for the formation of the carbon-nitrogen polymer PDCA.

Although the side-chains have conjugated bonds, the main carbon skeleton does not have a conjugated π-electron system, which is why the polymer is a dielectric. Several similar inorganic carbon-nitrogen polymers are known, such as paracyanogen $(NCCN)_x$, paraisocyanogen $(CNCN)_x$, and polycyanogen $(NC(CN))_x$ [140,141]. Interestingly, paracyanogen, which contains polyaromatic cycles, is a semiconductor, but paraisocyanogen and polycyanogen are also dielectric materials [140,141].

In order to better understand the energy storage mechanism for the carbon│PDCA dielectric capacitors, *in situ* IRA spectra of the thin-film graphite│BMPyrrDCA system have been measured at different passivation potentials, shown in Fig. 25. It is seen that familiar wide ER peaks are measured, similar to the ER peaks for graphite│$EMImBF_4$ system when the capacitor is measured at passivation potential vs. reference potential at 0 V. The difference, however, is that both the negative going band as well as the positive band are observed. For the thin-film graphite│$EMImBF_4$ system the negative band could not be measured as the electronic energy level of graphite is close to zero at fermi level [126]. From the results shown in Fig. 25 it is interpreted that even for fully discharged graphite electrode passivated up to 2.5 V, the electronic energy is 0.2 eV and increases with passivation potential, up to 0.26 eV for passivation up to 7.5 V. Similarly, the positive-going band corresponding to the exited electronic states for the fully charged capacitor show increase in energy with passivation potential, from 0.29 eV at 2.5 V up to 0.35 eV at passivation potential of 7.5 V. That considered, the intensity of both bands decrease with an increase of passivation potential, suggesting that a lower number of electrons within the electronic band of graphite are excited when thickness of the dielectric layer increases. Table 5 shows the dependence of the ER peaks on passivation potential.

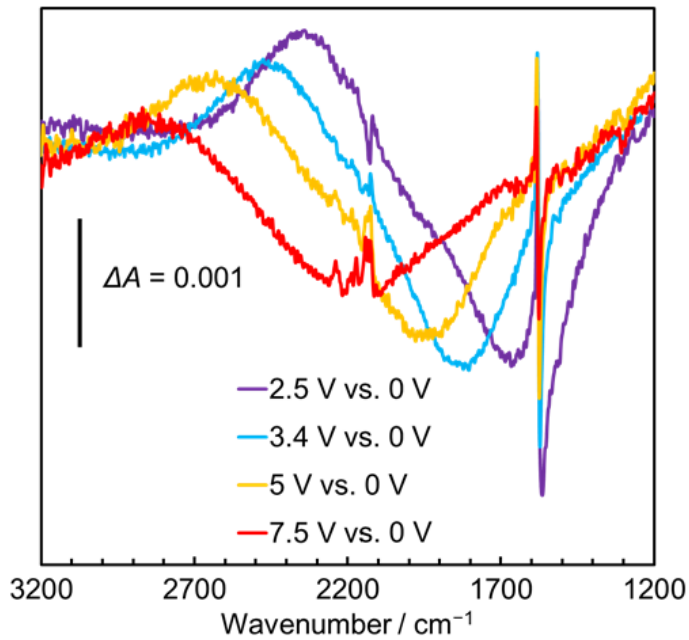

Figure 25. *In situ* IR spectra of the thin-film graphite on epoxy/ZnSe │PDCA interface measured with different passivation potentials relative to the reference potential at 0 V.

Table 5. Data for the electroreflectance peaks for the thin-film graphite │BMPyrrDCA system measured at different passivation potentials relative to reference potential at 0 V.

Passivation potential / V	E_{dip}^{1} / eV	E_{dip}^{2} / eV	ΔE_{dip} / eV
2.5	0.202	0.290	0.088
3.4	0.221	0.305	0.084
5	0.241	0.327	0.087
7.5	0.264	0.351	0.086
10	0.323	0.407	0.084

It is observed that although both the negative- and positive-going ER peaks shift to higher energy levels with increasing passivation potential, the difference between the peaks is relatively constant at approximately 0.085 eV. This suggests a fundamental limitation of the capacitor energy storage and is likely related to the dielectric constant of PDCA, which has been calculated to be between 6 and 10 for different layer thicknesses [71]. Also, based on the ER polarization slope for the graphite │$EMImBF_4$ system (0.233 eV V^{-1}) the polarization for the graphite │PDCA systems only corresponds to 0.36 V in the ideally polarizable potential scale. This, along with the lower number of exited electronic states explains the drastic drop in capacitance for the dielectric capacitors.

6.3. (VIII) Electrochemical behaviour of Bi(*hkl*)│PMImI interface

6.3.1. Analysis of CV data

Cyclic voltammograms for the Bi(*hkl*)│PMImI system [VIII] are shown in Fig. 26. It is seen that for the three different bismuth single crystal planes the voltammetry response is highly similar: the negative potential limit is indistinguishable, as this describes fundamentally the same cation decomposition process as that shown for the thin film Bi interface with $EMImBF_4$ ionic liquid [142]. It should also be noted that the potential at which this process takes place is the same as that for both the thin film Bi and amorphous carbon in $EMImBF_4$ [56,142], suggesting that the reduction process on these electrodes is fundamentally limited by the electron transfer to the imidazolium cation lowest unoccupied electronic state with no catalytic effects. In the case of highly oriented pyrolytic graphite (HOPG) [54] or thin layer Pb electrodes [110] the negative potential limit faradic process can be observed at a significantly less negative potential, likely because it corresponds to a different reaction (intercalation of cations into graphite structure in case of HOPG) or due to catalytic effects regarding the hydrogen evolution process that takes place at the Pb interface [110].

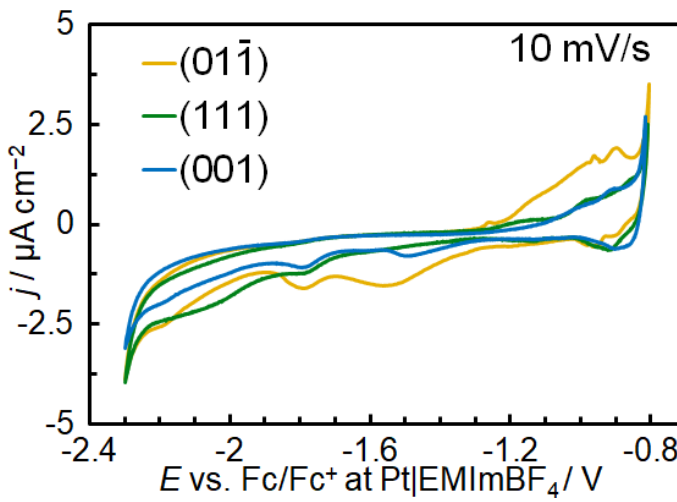

Figure 26. Cyclic voltammograms for the Bi(*hkl*)│PMImI systems within the ideal polarizability region.

At the positive potential limit the three Bi planes also show similar behaviour, with a sharp increase of positive current density observed at −0.8 V and a small reduction peak (i.e. re-reduction) immediately following for the reverse scan, suggesting that an oxidation process that is at least quasi-reversible is taking

place. In general, there are two different oxidation processes that can be related to either the oxidation of iodide anions into triiodide anions (I_3^-) or the dissolution of the bismuth electrode. Both processes are either reversible or quasi-reversible in nature and are thus difficult to differentiate between with only applying the CV method. It is also possible that both processes are taking place simultaneously with varying degrees of intensity between them. However, it should be mentioned that because the activation potential of this process does not significantly vary for the three Bi single crystal planes suggests that this process is not, at least primarily, Bi dissolution. Another factor to consider is that the dissolution of Bi thin films in non-halogen ionic liquid ($EMImBF_4$) was observed at a significantly higher positive potential value [142], leading to a wider electrochemical stability range (2.1 V) than the value observed for the PMImI ionic liquid (1.55 V). Considering this, it is also possible that the interaction of iodide ions can play a significant role in stabilizing the dissolved Bi cations (Bi^{3+}) and thus play a catalytic role in the corrosion of the Bi electrodes. This effect cannot, however, be adequately evaluated by electrochemical measurements alone and thus *in situ* STM measurements would be required.

6.3.2. Analysis and modelling of EIS data

EIS along with electrical equivalent circuit analysis was applied within the range of −2.28 to −0.83 V for the Bi(*hkl*) | PMImI systems.

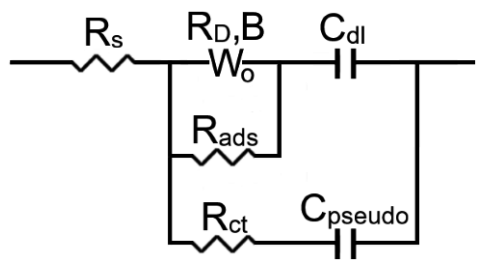

Figure 27. Electrical equivalent circuit used for the fitting of the impedance data.

EIS EC fitting process has been applied to the Bi(*hkl*) | PMImI systems and an equivalent circuit has been derived, shown in Fig. 27. It should be noted that not all components of the EC can be quantified within the whole frequency and potential ranges measured and thus some components have been omitted when the role of the process that they correspond to is too small. Overall, the EC is described by 6 elements corresponding to 7 free parameters denoting a system with two time-constants. R_S corresponds to the solution resistance which describes the overall electric resistance as well as the solution layer resistance

between the electrode and Luggin capillary. This parameter should not strongly depend on the potential applied if the resistance of the dielectric medium is constant. R_{ads} corresponds to the resistance of the specific adsorption process of iodide ions on the Bi electrode surface. This parameter should decrease when more positive electrode potential is applied. In parallel with the adsorption resistance Warburg like semifinite-length diffusion element W_o describes the mass-transfer limited movement of adsorbing ionic species in a thin interface layer. This element is required because of the high viscosity and low diffusion coefficient [62] of the PMImI ionic liquid ions. The mass-transfer limited element is used in the classical form with the value of α fixed at 0.5 and is thus described by two free parameters: mass-transfer resistance R_D and mass-transfer time constant T_{war} that describes the time taken for the diffusing particles to move through the thin layer. This means that by knowing the diffusion constant of relevant species, the thickness of the thin layer can be evaluated [144]. In series with both the mass-transfer and adsorption resistance components is the electrical double layer capacitance C_{dl}. This is the primary component whereby the capacitive charge storage of the system can be evaluated.

Two additional elements in parallel with the previous three components describe the low-frequency end of the impedance spectrum, as shown in Fig. 27. Charge-transfer resistance, R_{ct}, characterises faradic charge transfer processes involving either low-concentration impurities or the ions of the ionic liquid themselves. This element can describe many different reactions that take place at different potential values, but will always primarily describe the fastest process taking place at a selected fixed potential. Thus, at the most negative potential region, it will show the reduction of $PMIm^+$ cations and at the positive potential region show the oxidation of iodide ions. If the process ascribed by the R_{ct} component is either reversible or quasi-reversible, the pseudo-capacitive term, C_{pseudo}, is added in series with R_{ct} to evaluate the energy storage ability of the faradic reaction. Again, although this term should be evaluated in terms of capacity, the parameter is still shown in capacitance units (thus the name-capacitance-like). This element is not used at more negative potentials ($E < -1.1$ V) as the reactions taking place at more negative potentials are not reversible.

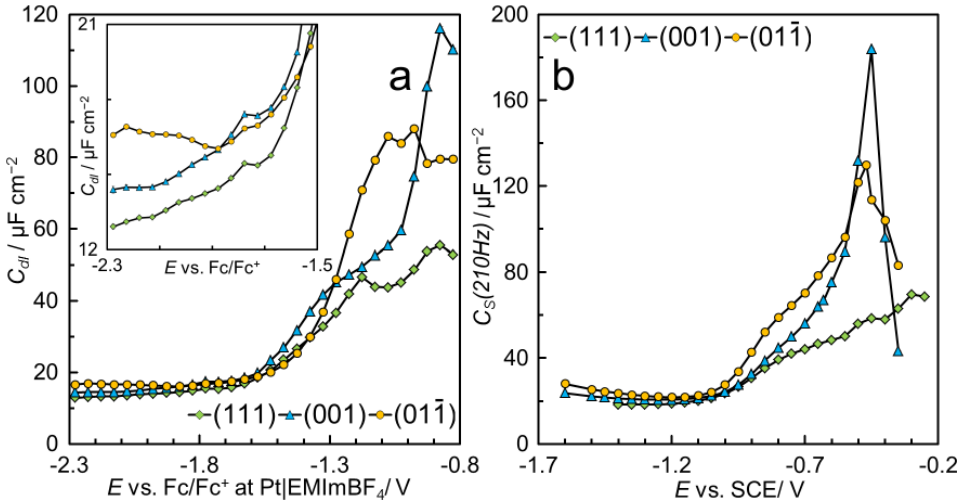

Figure 28. Electrical double layer capacitance C_{dl} vs. E dependence for the Bi(*hkl*) | PMImI systems (a) and cut-out of the electrostatic double layer potential range (inset a); series capacitance C_S vs. E dependence for the Bi(*hkl*) | 0.1 M KI aqueous electrolyte systems (b).

The electrical double layer capacitance for the Bi(*hkl*) | PMImI systems, obtained from EC fitting results, are shown in Fig. 28a. Each of the EC fitting parameters carries with it an error value based on the goodness of fit for that specific parameter. It is seen that the error values for the C_{dl} parameter are extremely low and thus almost unnoticeable in the figure. The negative-potential region cut-out of the same graph is shown in the inset of Fig. 28a. It is seen that the data can be divided into two distinct areas of more and less negative electrode potential. In the more negative electrode potential region from −2.3 to approximately −1.4 V the value of capacitance is relatively low (between 12 and 25 μF cm^{-2}) and the general behaviour of the three electrodes is similar. However, one can still easily detect that the capacitance of the most metallic Bi(01$\bar{1}$) plane is appreciatively higher than that of the least metallic Bi(111) plane (17 vs. 14 μF cm^{-2} in the potential region from −2.3 to −1.7 V) while the Bi(001) plane with average metallic character fits between the previous two planes. Thus the capacitance follows the same general rule as that observed for aqueous electrolytes, whereby higher metallicity of the electrode material correlates well with the double layer capacitance response of the dense layer [145]. This is of great interest because such general trend, based on the available literature, is not followed in case of perceived surface inactive ionic liquid $EMImBF_4$, whereby the average double layer capacitance at the minimum decreases in the order of Sb(111) [146] > Bi(111) [147] ~ Hg(liquid) [148] > Cd(0001) [149]. It is unknown as to how one might explain such difference for metal electrodes. However, the same effect does not apply for carbon based materials (perceived as least metallic) that show capacitance

significantly lower than that of metals [56,143], clearly limited by their charge carrier concentration at a given potential. If such an effect is indeed true, it would signify that carrier concentration is not the primary limiting factor in the screening of the double layer electric field for most metals in an ionic liquid media. Clearly, this is not the case for our Bi(*hkl*) single crystal planes whereby metallicity is important to consider even in the electrostatic double layer region.

Even more interesting is the potential range from −1.3 to −0.8 V, where the difference in the double layer capacitance response for the three Bi electrodes is more pronounced. Whereas the most semi-metallic Bi(111) plane shows a relatively constant increase of capacitance in this region with a maximum of about 55 μF cm^{-2}, the more metallic (001) and (01$\bar{1}$) planes show a significantly sharper increase of capacitance and maxima of 115 and 87 μF cm^{-2} have been measured, respectively. This effect is perceived to be the result of the interaction between the electronic and ionic surface structure, resulting from partial charge transfer from the iodide ions of the electrolyte to conduction band of the Bi(*hkl*) electrode. Because each single crystal plane has a distinct surface electronic structure, this effect is more pronounced for electrodes with higher number of free electronic states (metals) and less pronounced for semi-metals with a relatively low concentration of valence electronic states. In the case of the three Bi single crystal electrodes that are all semi-metallic in nature with a varying degree of metallicity, the measurement of capacitance clearly shows the difference between the three different planes and provides information about the relative band structure of each electrode.

In order better understand this effect of electronic capacitance on the overall capacitance response, the same three Bi single crystals were measured in a more typical, 0.1 M KI aqueous electrolyte solution [69,70]. The series capacitance results of the Bi(*hkl*) | 0.1M KI in H_2O measured at 210 Hz are shown in Fig. 28b. It should be noted that although the single frequency series capacitance results are less accurate than EC fitting of the C_{dl} element, they can still well represent the EDL capacitance if the frequency value at which they are measured is well-chosen. The chosen C_S ac frequency is significantly higher for the aqueous electrolyte solution because of the differences in viscosity and conductivity between the two electrolytes. As observed by comparing the *C*, *E* curves in Fig. 28 a and b, many similarities are found. The *C*, *E* curve for the KI system can also be generally divided into two parts of differing capacitance behaviour, and the general logic between the three different single crystal planes also holds true. The overall values of the capacitance maxima are up to 50% larger for the aqueous electrolyte compared to PMImI ionic liquid, but is compensated by the narrower electrochemical stability range, meaning that the absolute surface charge density values are similar. It is also evident that the *C*, *E* curves for the least metallic Bi(111) plane are most similar between the PMImI and 0.1M KI in H_2O electrolytes with only 10% difference between the capacitance maxima and comparable linear increase of capacitance in the less negative potential range, where the specific adsorption of iodide ions has been observed. The most likely explanation for this effect is that the *C*,*E* curves are

mainly limited by the electronic response of the electrode material and thus behave in a similar manner as that observed for HOPG electrodes [54], whereby the difference between the capacitance response is very small for both electrolyte concentration, solvent or the absence of a solvent. The differences between the more metallic Bi planes are more significant for the two electrolytes, however, still show general features that are comparable for the PMImI and 0.1M KI electrolytes.

Finally, it is interesting to observe the electrode potential dependence of the resistive components of the EC fitting, shown in Fig. 29. The solution resistance R_S is primarily determined by the distance between the working electrode and reference electrode capillary as well as the electrolyte conductivity, both of which are inherently constant for our measurements and should thus reveal no strong dependence of R_S on electrode potential. This, however, ignores the possibility of changes in the electrolyte composition under electrochemical polarization, which could have a significant contribution on the overall electrolyte resistance. It is seen in Fig. 29a that indeed there is no specific dependence of R_S on the Bi single crystal plane, as the measurements were conducted in fundamentally the same fashion and the resistance is relatively constant, considering fitting error, within the potential range from −2.3 to −1.2 V. Thereafter, however, R_S starts to decrease rapidly with potential at $E > -1.2$ V for all Bi electrodes. This effect is again interpreted to stem from the behaviour of iodide ions in a solution. Because of the high viscosity, the diffusion coefficient of iodide ions in the PMImI ionic liquid is very low, about $1.9 \cdot 10^{-12}$ $m^2\ s^{-1}$ [62]. However, if molecular iodine were added to the solution, as is the case when the same ionic liquid is used as an electrolyte in a DSSC, triiodide ions would be formed [152]. As is known from literature, in an electrolyte composed of both iodide and triiodide ions the conductivity can be significantly enhanced because of an alternative conduction path – the hopping of iodide ions from one complex to another [72]. This mechanism has been shown to have a diffusion coefficient on the order of 10^{-9} $m^2\ s^{-1}$ [62,72], thus 3 orders of magnitude higher than that of pure iodide in PMImI. At less negative potential ($E > -1.2$ V) iodide ions can be oxidized into triiodide ions, as shown by the CV measurements. This can therefore create a parallel conduction mechanism for the electrolyte resistance and it is likely the reason as to why we observe a rapid, linear decrease of the R_S parameter for our systems. The overall decrease is up to 8% for the Bi(111) electrode, suggesting that a considerable amount of free triiodide ions have been formed, diffused into the bulk electrolyte and reduced at the counter-electrode.

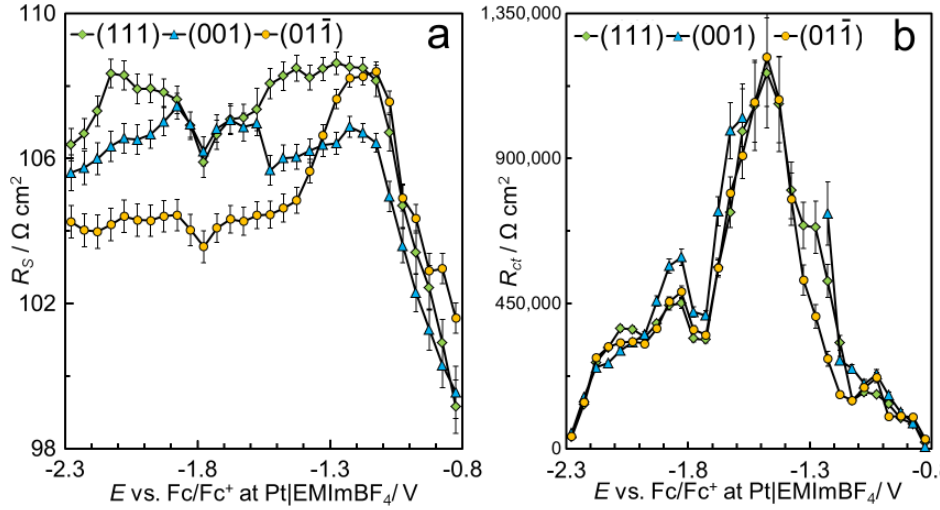

Figure 29. Calculated fitting parameters of Nyquist plots for the Bi(*hkl*) | PMImI systems; solution resistance R_S (a) and charge-transfer resistance R_{ct} (b) vs. E dependence.

The resistance of low frequency charge transfer process (R_{ct}) is shown in Fig. 29b. The process to which this parameter corresponds to changes with applied electrode potential, and from −1.6 V to −1.3 V no significant charge transfer processes are taking place at the Bi(*hkl*) electrode surface, thus contributing to the high fitting error in this potential region. For potentials more negative than −2.1 V this process corresponds to the reduction of imidazolium cations [56] discussed beforehand. Within the potential region from −2.1 to −1.6 V, the reduction of trace water impurities is interpreted to be the main cause of R_{ct} [147]. At electrode potential values above −1.3 V, R_{ct} characterises the slow redox processes, causing also the quasi-reversible peaks in the CV curves and increase in the values of C_{pseudo}. No specific dependence of R_{ct} on the Bi(*hkl*) planes is observed as the faradic resistance of these processes mostly overlap for the three Bi single crystal planes suggesting that the chemical nature of Bi is more influential on these processes compared to both the surface electronic structure and the ionic structure of the EDL, supported by the similarities between the Bi planes in CV and EIS resistance parameters.

6.4. (I-VIII) Considerations of the EDL

Theoretical and modelling approaches have been by far the most proactive in trying to explain the charge screening properties of ionic liquids. A large number of different approaches have been taken, ranging from extensions of the diffuse double layer theory [16,17] up to extensive molecular dynamics (MD) simulations with different electrolyte geometries, electrodes and temperatures

[27–29]. A major drawback to almost all of the MD based studies is the complete exclusion of electronic effects of the EDL, such as the work function difference between the electrode and the electrolyte [14], electronic structure of the electrode, partial charge transfer between ions and the electrode as well as the association of the ions. This is exemplified by the way potential is treated for polarizable and non-polarizable systems [30]. Thus, the results of these theoretical approaches cannot be considered reliable at potentials near the pzc where the discrepancy in electrode | electrolyte work function difference is highest. Most of these models are in general agreement about the capacitive behaviour at high surface charge densities, as they show a slow decrease of capacitance at the potential 'wings' (extrema). It can be suggested that at high surface charge density, the strong electric fields are enough to overcome the association between ions within the compact layer and thus a hard spheres approach would be sufficient to characterize the essential physics of the interface, however, the limitation of the region of ideal polarizability for $EMImBF_4$ ionic liquid will not allow us to gauge that.

It is thus seen that the consideration of specific interactions (both between the ions and between the ions and the electrode surface) within an IL is extremely important in trying to explain the capacitive behaviour of metal | IL interfaces, which has been exemplified in this thesis. By considering the association between ions in ILs, we are able to explain the results of this study as well as consider many of the discrepancies observed in other experimental and theoretical studies. The results are also in good agreement with different AFM force-distance measurements [122,154] in ILs, showing pseudo-layering at IL interfaces, with layers approximately the thickness of ion pairs. This would suggest that dipole, not coulombic interactions are the most important part of the overall screening response of the electrolyte at low surface charge densities. These pseudo-layers can also be 'turned around' in order to screen positive or negative surface charge, and a thickening of the structured electrolyte layer would be consistent with the increase of capacitance relative to the pzc. Nonetheless, as is observed by the SEIRA measurements shown in this study, there is a finite range of electrode potential wherein this consideration is applicable. Because of the strong electric fields at high surface charge densities, the strength of ion association between the ions is seen to decrease considerably and thus the capacitance is also seen to decrease at the wings, giving rise to coulombic screening response of the electrolyte. It can be suggested that at extreme surface charge densities, whereupon all of the ionic association between the ions in the dense layer has been overcome, the description of hard-sphere ILs would be sufficient in explaining the overall capacitance response of the interface.

As it was shown by *in situ* ER spectroscopy results, the mechanism of energy storage for the dielectric graphite | PDCA system significantly differs from the purely electrostatic graphite | $EMImBF_4$ supercapacitor system [115,143]. Although this is not surprising, the exact mechanism of energy storage in dielectric capacitors, particularly from the view-point of conductor

electronic states, has not, thus far, been revealed. Such knowledge could help us in designing even higher energy density capacitors in the future by careful selection of both electrode materials and electrolyte components [139].

The measurements of specifically adsorbing iodide ions at Bi single crystal planes demonstrate that the capacitance of IL interfaces can be significantly increased via careful selection of electrolyte additives. However, it is also shown that this increase is highest for more metallic planes of semimetal Bi(*hkl*), thus limiting this effect for carbon based SC materials [155]. It should be noted, though, that these results clearly demonstrate that both the specific adsorption of iodide ions as well as the oxidation of iodide increase the energy storage capabilities of such systems [63].

At last, the shape of the *C, E* curve for the graphite | $EMImBF_4$ system and potential dependence of the *in situ* IRA spectra for the same system do not confirm the existence of multiple double layers, suggested by a theoretical article about the interface between graphite and an IL [35]. On the contrary, the experimental results suggest that more comprehensive models are required for a fundamental understanding of the complex processes at the electrode | IL interface.

7. SUMMARY

Atomic force microscopy, cyclic voltammetry, electrochemical impedance spectroscopy and *in situ* infrared (IR) absorption spectroscopy methods have been employed to study the electrical double layer (EDL) formation and charging processes for five different electrode materials of variable metallic properties. The electrochemistry measurements reveal the width of the region of ideal polarizability for the different materials in 1-ethyl-3-methylimidazolium tetrafluoroborate ($EMImBF_4$) ionic liquid (IL). The dependence of EDL capacitance on potential is shown to vary greatly between more metallic Au and Pb electrodes and semimetallic Bi, graphite and porous carbide derived carbon electrode. It is shown that for Pb and Au thin film electrodes, strong IR spectral signal enhancement in within the compact layer of the EDL permits us to probe the relative ion concentrations as well as orientations in the layer directly adjacent to the electrode surface. The semimetallic properties of Bi and graphite have a completely different enhancement of the IR spectral signal, showing absorption bands primarily originating from the diffuse layer of the EDL. More detailed analysis indeed confirms the existence of two distinct potential regions for the graphite │ $EMImBF_4$ system. It was determined that the *in situ* IR spectra for the thin-film graphite │ $EMImBF_4$ system not only allow us to probe the electrolyte side of the EDL but also the changes in the electronic structure of graphite. The in situ electroreflectance (ER) spectra show how the potential induced changes in the electronic structure of graphite.

A novel dielectric capacitor technology has been developed based on electropolymerizable dicyanamide anions. It is shown that flat, thin-film carbon electrodes are suitable for passivation up to 10 V in the 1-butyl-1-methyl-pyrrolidinium dicyanamide IL. It is shown that the formed dielectric polymer is a pure carbon-nitrogen compound polydicyanamide (PDCA). *In situ* ER spectroscopy measurements of the passivated graphite │ PDCA capacitors show that the energy storage mechanism is completely different from the ideally polarizable graphite │ $EMImBF_4$ system.

The EDL capacitance and interfacial resistance parameters were measured in a pure halide IL 1-propyl-3-methylimidazolium iodide (PMImI) for three Bi single crystal planes of variable metallic properties. It was shown that while the EDL capacitance is highly dependent on the Bi single crystal plane, particularly in the positive polarization range due to the specific adsorption of iodide ions, the interfacial resistance parameters do not show a strong dependence on the Bi(*hkl*) planes. More strikingly, it was shown that the EDL capacitance for Bi(*hkl*) │ PMImI systems correlate well with that of relatively dilute iodide ion containing aqueous solutions of the same planes, explained by the capacitive behaviour being dominated by the adsorbed iodide layer and surface electronic states of Bi single crystals.

8. REFERENCES

[1] H. Kurig, M. Vestli, K. Tõnurist, A. Jänes, E. Lust, J. Electrochem. Soc. 159 (2012) A944–A951.
[2] J.-D. Decoppet, S.B. Khan, M.S.A. Al-Ghamdi, B.G. Alhogbi, A.M. Asiri, S.M. Zakeeruddin, et al., Energy Technol. 5 (2017) 321–326.
[3] A. Volta, Phil Mag. 7 (1800).
[4] J. Ho, T.R. Jow, S. Boggs, IEEE Electr. Insul. Mag. 26 (2010) 20–25.
[5] H. von Helmholtz, Ann. Phys. 165 (1853) 211–233.
[6] G.L. Gouy, Lond. Edinburg Phil Mag J Sci. 25 (1910) 475.
[7] D.L. Chapman, Lond. Edinb. Dublin Philos. Mag. J. Sci. 25 (1913) 475–481.
[8] O. Stern, Zeit Elektrochem. 30 (1924) 508–516.
[9] O.K. Rice, Phys. Rev. 31 (1928) 1051–1059.
[10] A. Frumkin, A. Gorodetzkaja, Z. Für Phys. Chem. 136U (1928) 451–472.
[11] D.C. Grahame, Chem. Rev. 41 (1947) 441–501.
[12] H. Gerischer, Electrochimica Acta. 35 (1990) 1677–1699.
[13] H. Gerischer, J. Phys. Chem. 89 (1985) 4249–4251.
[14] B.B. Damaskin, O.A. Petrii, J. Solid State Electrochem. 15 (2011) 1317–1334.
[15] E. Lust, Electrical Double Layers. Double Layers at Single-crystal and Polycrystalline Electrodes, in: A. J. Bard, M. Stratmann, E. Gileadi, M. Urbakh (Eds.), Encycl. Electrochem. Thermodyn. Electrified Interfaces, Wiley VCH, 2002: pp. 188–225.
[16] A.A. Kornyshev, J. Phys. Chem. B. 111 (2007) 5545–5557.
[17] K.B. Oldham, J. Electroanal. Chem. 613 (2008) 131–138.
[18] M.Z. Bazant, B.D. Storey, A.A. Kornyshev, Phys. Rev. Lett. 106 (2011) 046102.
[19] T. Pajkossy, D.M. Kolb, Electrochem. Commun. 13 (2011) 284–286.
[20] L. Siinor, C. Siimenson, V. Ivaništšev, K. Lust, E. Lust, J. Electroanal. Chem. 668 (2012) 30–36.
[21] M.T. Alam, J. Masud, M.M. Islam, T. Okajima, T. Ohsaka, J. Phys. Chem. C. 115 (2011) 19797–19804.
[22] V. Lockett, R. Sedev, J. Ralston, M. Horne, T. Rodopoulos, J. Phys. Chem. C. 112 (2008) 7486–7495.
[23] V. Lockett, M. Horne, R. Sedev, T. Rodopoulos, J. Ralston, Phys. Chem. Chem. Phys. 12 (2010) 12499–12512.
[24] F. Silva, C. Gomes, M. Figueiredo, R. Costa, A. Martins, C.M. Pereira, J. Electroanal. Chem. 622 (2008) 153–160.
[25] R. Costa, C.M. Pereira, A.F. Silva, Electrochimica Acta. 167 (2015) 421–428.
[26] L. Siinor, K. Lust, E. Lust, Electrochem. Commun. 12 (2010) 1058–1061.
[27] M.V. Fedorov, N. Georgi, A.A. Kornyshev, Electrochem. Commun. 12 (2010) 296–299.
[28] M.V. Fedorov, A.A. Kornyshev, J. Phys. Chem. B. 112 (2008) 11868–11872.
[29] J. Vatamanu, O. Borodin, G.D. Smith, J. Am. Chem. Soc. 132 (2010) 14825–14833.
[30] E. Paek, A.J. Pak, G.S. Hwang, J. Chem. Phys. 142 (2015) 024701.
[31] V. Ivaništšev, M.V. Fedorov, Electrochem. Soc. Interface. 23 (2014) 65–69.
[32] M. Salanne, L.J.A. Siqueira, A.P. Seitsonen, P.A. Madden, B. Kirchner, Faraday Discuss. 154 (2011) 171–188.
[33] E. Paek, A.J. Pak, G.S. Hwang, J. Electrochem. Soc. 160 (2013) A1–A10.

[34] Z. Hu, J. Vatamanu, O. Borodin, D. Bedrov, Phys. Chem. Chem. Phys. 15 (2013) 14234–14247.
[35] A.A. Kornyshev, N.B. Luque, W. Schmickler, J. Solid State Electrochem. 18 (2014) 1345–1349.
[36] Y. Lauw, M.D. Horne, T. Rodopoulos, F.A.M. Leermakers, Phys. Rev. Lett. 103 (2009) 117801–4.
[37] Y. Lauw, M.D. Horne, T. Rodopoulos, A. Nelson, F.A.M. Leermakers, J. Phys. Chem. B. 114 (2010) 11149–11154.
[38] Z.A. Goodwin, G. Feng, A.A. Kornyshev, Electrochimica Acta. 225 (2017) 190–197.
[39] A.A. Kornyshev, R. Qiao, J. Phys. Chem. C. 118 (2014) 18285–18290.
[40] M.V. Fedorov, A.A. Kornyshev, Chem. Rev. 114 (2014) 2978–3036.
[41] M. Salanne, Phys. Chem. Chem. Phys. 17 (2015) 14270–14279.
[42] F. Faridbod, M.R. Ganjali, P. Norouzi, S. Riahi, H. Rashedi, Application of Room Temperature Ionic Liquids in Electrochemical Sensors and Biosensors, in: A. Kokorin (Ed.), Ion. Liq. Appl. Perspect., InTech, Croatia, 2011: pp. 643–657.
[43] P. Walden, Chem Zentralbl. 85 (1914) 1800–1801.
[44] W.W. Liu, L.Y. Cheng, Y.M. Zhang, H.P. Wang, M.F. Yu, J. Mol. Liq. 140 (2008) 68–72.
[45] F. Endres, S.Z. El Abedin, Phys. Chem. Chem. Phys. 8 (2006) 2101–2116.
[46] O.O. Okoturo, T.J. Van der Noot, J. Electroanal. Chem. 568 (2004) 167–181.
[47] T.Y. Yan, S. Li, W. Jiang, X.P. Gao, B. Xiang, G.A. Voth, J. Phys. Chem. B. 110 (2006) 1800–1806.
[48] H. Ohno, ed., Electrochemical Aspects of Ionic Liquids, Wiley & Sons, 2005.
[49] M. Armand, F. Endres, D.R. MacFarlane, H. Ohno, B. Scrosati, Nat. Mater. 8 (2009) 621–629.
[50] M. Galinski, A. Lewandowski, I. Stepniak, Electrochimica Acta. 51 (2006) 5567–5580.
[51] H. Liu, Y. Liu, J. Li, Phys. Chem. Chem. Phys. 12 (2010) 1685–1697.
[52] G. Boschloo, A. Hagfeldt, Acc. Chem. Res. 42 (2009) 1819–1826.
[53] K.N. Marsh, A. Deev, A.C.-T. Wu, E. Tran, A. Klamt, Korean J. Chem. Eng. 19 (2002) 357–362.
[54] J.S. Wilkes, M.J. Zaworotko, Chem. Commun. 13 (1992) 965–967.
[55] T. Romann, O. Oll, P. Pikma, E. Lust, Electrochem. Commun. 23 (2012) 118–121.
[56] T. Romann, O. Oll, P. Pikma, H. Tamme, E. Lust, Electrochimica Acta. 125 (2014) 183–190.
[57] K. Kubo, N. Hirai, T. Tanaka, S. Hara, Surf. Sci. 546 (2003) L785–L788.
[58] Y. Liu, Y.-X. Yuan, X.-R. Wang, N. Zhang, M.-M. Xu, J.-L. Yao, et al., J. Electroanal. Chem. 728 (2014) 10–17.
[59] N. Nanbu, Y. Sasaki, F. Kitamura, Electrochem. Commun. 5 (2003) 383–387.
[60] N. Nanbu, T. Kato, Y. Sasaki, F. Kitamura, Electrochemistry. 73 (2005) 610–613.
[61] C. Siimenson, M. Lembinen, O. Oll, L. Läll, M. Tarkanovskaja, V. Ivaništšev, et al., J. Electrochem. Soc. 163 (2016) H723–H730.
[62] H. Kurig, A. Jänes, E. Lust, J. Electrochem. Soc. 157 (2010) A272–A279.
[63] L. Siinor, J. Poom, C. Siimenson, K. Lust, E. Lust, J. Electroanal. Chem. 719 (2014) 133–137.
[64] R. Palm, H. Kurig, K. Tõnurist, A. Jänes, E. Lust, Electrochimica Acta. 85 (2012) 139–144.

[65] R. Palm, H. Kurig, K. Tonurist, A. Janes, E. Lust, J. Electrochem. Soc. 160 (2013) A1741–A1745.
[66] M.Y. Lui, L. Crowhurst, J.P. Hallett, P.A. Hunt, H. Niedermeyer, T. Welton, Chem. Sci. 2 (2011) 1491.
[67] T. Nishida, Y. Tashiro, M. Yamamoto, J. Fluor. Chem. 120 (2003) 135–141.
[68] Y. Bai, Y. Cao, J. Zhang, M. Wang, R. Li, P. Wang, et al., Nat. Mater. 7 (2008) 626–630.
[69] Z. Fei, D. Kuang, D. Zhao, C. Klein, W.H. Ang, S.M. Zakeeruddin, et al., Inorg. Chem. 45 (2006) 10407–10409.
[70] D.R. MacFarlane, S.A. Forsyth, J. Golding, G.B. Deacon, Green Chem. 4 (2002) 444–448.
[71] T. Romann, O. Oll, P. Pikma, K. Kirsimäe, E. Lust, J. Power Sources. 280 (2015) 606–611.
[72] P.A. Christensen, In situ Infrared Spectroelectrochemistry, in: A.J. Bard, M. Stratmann, P.R. Unwin (Eds.), Encycl. Electrochem. Instrum. Electroanal. Chem., Wiley VCH, 2003: pp. 530–571.
[73] M. Osawa, Surface-Enhanced Infrared Absorption Spectroscopy, in: Handb. Vib. Spectrosc., John Wiley & Sons, Ltd, 2006.
[74] F.W. Richey, B. Dyatkin, Y. Gogotsi, Y.A. Elabd, J. Am. Chem. Soc. 135 (2013) 12818–12826.
[75] Y.-Q. Bie, J. Horng, Z. Shi, L. Ju, Q. Zhou, A. Zettl, et al., Nat. Commun. 6 (2015).
[76] B.C. Smith, Fundamentals of Fourier transform infrared spectroscopy, CRC Press, Boca Raton, 1996.
[77] T. Vo-Dinh, G. Gauglitz, Handbook of spectroscopy, Wiley-VCH, Weinheim, 2003.
[78] K. Ashley, S. Pons, Chem. Rev. 88 (1988) 673–695.
[79] A. Hartstein, J.R. Kirtley, J.C. Tsang, Phys. Rev. Lett. 45 (1980) 201–204.
[80] M. Osawa, Bull. Chem. Soc. Jpn. 70 (1997) 2861–2880.
[81] R.G. Greenler, D.R. Snider, D. Witt, R.S. Sorbello, Surf. Sci. 118 (1982) 415–428.
[82] K. Ataka, D. Mayer, T. Wandlowski, Langmuir. 18 (2002) 4331–4341.
[83] S.-J. Huo, J.-Y. Wang, D.-L. Sun, W.-B. Cai, Appl. Spectrosc. 63 (2009) 1162–1167.
[84] V. Grozovski, V. Ivaništšev, H. Kasuk, T. Romann, E. Lust, Electrochimica Acta. 120 (2014) 86–95.
[85] R. Aroca, B. Price, J. Phys. Chem. B. 101 (1997) 6537–6540.
[86] Q.-X. Li, X.-K. Xue, Q.-J. Xu, W.-B. Cai, Appl. Spectrosc. 61 (2007) 1328–1333.
[87] T. Romann, Preparation and surface modification of bismuth thin film, porous, and microelectrodes, Thesis, 2010.
[88] M. Osawa, K.-I. Ataka, K. Yoshii, Y. Nishikawa, Appl. Spectrosc. 47 (1993) 1497–1502.
[89] V. Grozovski, V. Ivaništšev, H. Kasuk, T. Romann, E. Lust, Electrochimica Acta. 120 (2014) 86–95.
[90] P. Pikma, H. Kasuk, O. Oll, V. Ivaništšev, T. Romann, V. Grozovski, E. Lust, Adsorption of 4,4′-bipyridine on the Cd(0001) single crystal electrode surface, Electrochimica Acta, 180, 965−976 (2015).
[91] N. Nishi, K. Minami, K. Motobayashi, M. Osawa, T. Sakka, J. Phys. Chem. C. 121 (2017) 1658–1666.

[92] K. Motobayashi, N. Nishi, Y. Inoue, K. Minami, T. Sakka, M. Osawa, J. Electroanal. Chem. 800 (2017) 126-133.
[93] K. Motobayashi, K. Minami, N. Nishi, T. Sakka, M. Osawa, J. Phys. Chem. Lett. 4 (2013) 3110–3114.
[94] A.J. Bard, L.R. Faulkner, Electrochemical methods: fundamentals and applications, Wiley, New York, 2001.
[95] W. Schmickler, E. Santos, Interfacial Electrochemistry, 2nd ed., Springer, New York, 2010.
[96] B. Speiser, Linear Sweep and Cyclic Voltammetry, in: Encycl. Electrochem. Instrum. Electroanal. Chem., Wiley, New York, 2003: pp. 81–104.
[97] J.O. Bockris, A.K.N. Reddy, M. Gamboa-Aldeco, Modern electrochemistry: Volume 2A, 2nd ed., Kluwer Academic Publishers, New York, 2002.
[98] P.T. Kissinger, W.R. Heineman, J. Chem. Educ. 60 (1983) 702.
[99] K. Jüttner, W.J. Lorenz, Mater. Sci. Forum. (1989).
[100] A. Lasia, Electrochemical impedance spectroscopy and its applications, in: Mod. Asp. Electrochem., Springer, 2002: pp. 143–248.
[101] A.J. Bard, M. Stratmann, P.R. Unwin, eds., Encyclopedia of Electrochemistry: Instrumentation and Electroanalytical Chemistry v. 3, Wiley VCH, 2003.
[102] EIS Equivalent Circuits, in: Electrochem. Impedance Spectrosc. PEM Fuel Cells, Springer, London, 2010: pp. 139–192.
[103] T. Pajkossy, R. Jurczakowski, Curr. Opin. Electrochem. 1 (2017) 53–58.
[104] O. Oll, T. Romann, P. Pikma, E. Lust, J. Electroanal. Chem. 778 (2016) 41–48.
[105] O. Oll, C. Siimenson, K. Lust, G. Gorbatovski, E. Lust, Electrochimica Acta. 247 (2017) 910–919.
[106] O. Oll, T. Romann, E. Lust, Electrochem. Commun. 46 (2014) 22–25.
[107] A. Jänes, T. Thomberg, H. Kurig, E. Lust, Carbon. 47 (2009) 23–29.
[108] S. Brunauer, L.S. Deming, W.E. Deming, E. Teller, J. Am. Chem. Soc. 62 (1940) 1723–1732.
[109] M.J. Frisch, G.W. Trucks, H.B. Schlegel, G.E. Scuseria, M.A. Robb, J.R. Cheeseman, et al., Gaussian 09 Revision C, 2009.
[110] O. Oll, T. Romann, P. Pikma, E. Lust, J. Electroanal. Chem. 778 (2016) 41–48.
[111] E. Lust, G. Nurk, A. Jänes, M. Arulepp, L. Permmann, P. Nigu, et al., Condens. Matter Phys. 5 (2002) 307–327.
[112] N.B. Luque, W. Schmickler, Electrochimica Acta. 71 (2012) 82–85.
[113] C. Müller, S. Vesztergom, T. Pajkossy, T. Jacob, J. Electroanal. Chem. 737 (2015) 218–225.
[114] I.S. Perelygin, M.A. Klimchuk, J. Appl. Spectrosc. 50 (1989) 207–211.
[115] T. Romann, O. Oll, P. Pikma, H. Tamme, E. Lust, Electrochimica Acta. 125 (2014) 183–190.
[116] N.E. Heimer, R.E. Del Sesto, Z. Meng, J.S. Wilkes, W.R. Carper, J. Mol. Liq. 124 (2006) 84–95.
[117] T. Romann, O. Oll, P. Pikma, E. Lust, Electrochem. Commun. 23 (2012) 118–121.
[118] M.A. Gebbie, M. Valtiner, X. Banquy, E.T. Fox, W.A. Henderson, J.N. Israelachvili, Proc. Natl. Acad. Sci. 110 (2013) 9674–9679.
[119] A.A. Lee, D. Vella, S. Perkin, A. Goriely, J. Phys. Chem. Lett. 6 (2015) 159–163.
[120] M. Thomas, M. Brehm, O. Hollóczki, Z. Kelemen, L. Nyulászi, T. Pasinszki, et al., J. Chem. Phys. 141 (2014) 024510.

[121] E.N. Gribanov, O.I. Markov, Y.V. Khripunov, Nanotechnologies Russ. 6 (2011) 593.
[122] X. Zhang, Y.-X. Zhong, J.-W. Yan, Y.-Z. Su, M. Zhang, B.-W. Mao, Chem Commun. 48 (2011) 582–584.
[123] F. Endres, N. Borisenko, S.Z.E. Abedin, R. Hayes, R. Atkin, Faraday Discuss. 154 (2012) 221–233.
[124] D.M. Kolb, UV-visible reflectance spectroscopy, in: Spectroelectrochemistry, Springer, 1988: pp. 87–188.
[125] D.M. Kolb, W.N. Hansen, Surf. Sci. 79 (1979) 205–211.
[126] B. Partoens, F.M. Peeters, Phys. Rev. B. 74 (2006) 075404.
[127] D.M. Kolb, C. Franke, Appl. Phys. A. 49 (1989) 379–387.
[128] J.-H. Zhong, J.-Y. Liu, Q. Li, M.-G. Li, Z.-C. Zeng, S. Hu, et al., Electrochimica Acta. 110 (2013) 754–761.
[129] F. Rana, Nanotechnol. IEEE Trans. On. 7 (2008) 91–99.
[130] L. Ju, B. Geng, J. Horng, C. Girit, M. Martin, Z. Hao, et al., Nat Nano. 6 (2011) 630–634.
[131] Y. Li, H. Yan, D.B. Farmer, X. Meng, W. Zhu, R.M. Osgood, et al., Nano Lett. 14 (2014) 1573–1577.
[132] A.N. Grigorenko, M. Polini, K.S. Novoselov, Nat. Photonics. 6 (2012) 749–758.
[133] J.-P. Randin, E. Yeager, J. Electrochem. Soc. 118 (1971) 711–714.
[134] O. Oll, T. Romann, C. Siimenson, E. Lust, Electrochem. Commun. 82 (2017) 39–42.
[135] P. Reichert, K. Skov Kjær, T.B. van Driel, J. Mars, J. Walther Ochsmann, D. Pontoni, et al., Faraday Discuss. (2017).
[136] F. Kaasik, T. Tamm, M.M. Hantel, E. Perre, A. Aabloo, E. Lust, et al., Electrochem. Commun. 34 (2013) 196–199.
[137] J. Torop, M. Arulepp, T. Sugino, K. Asaka, A. Jänes, E. Lust, et al., Langmuir. 30 (2014) 2583–2587.
[138] T. Romann, E. Anderson, P. Pikma, H. Tamme, P. Möller, E. Lust, Electrochem. Commun. 74 (2017) 38–41.
[138] T. Romann, E. Lust, O. Oll, Method of Forming a Dielectric Through Electrodeposition on an Electrode for a Capacitor, WO/2016/050761, 2016.
[140] L.W. Jenneskens, J.W.G. Mahy, E.J. Vlietstra, S.J. Goede, F. Bickelhaupt, J. Chem. Soc. Faraday Trans. 90 (1994) 327–332.
[141] Z. Tóth, J. Gulyás, M.T. Beck, Inorganica Chim. Acta. 113 (1986) 67–70.
[142] T. Romann, O. Oll, P. Pikma, E. Lust, Electrochem. Commun. 23 (2012) 118–121.
[143] O. Oll, T. Romann, E. Lust, Electrochem. Commun. 46 (2014) 22–25.
[144] T. Jacobsen, K. West, Electrochimica Acta. 40 (1995) 255–262.
[145] R. Parsons, Chem. Rev. 90 (1990) 813–826.
[146] P. Pikma, L. Siinor, O. Oll, E. Lust, Electrochem. Commun. 61 (2015) 61–65.
[147] L. Siinor, K. Lust, E. Lust, J. Electrochem. Soc. 157 (2010) F83–F87.
[148] M.T. Alam, M.M. Islam, T. Okajima, T. Ohsaka, J. Phys. Chem. C. 111 (2007) 18326–18333.
[149] V. Ivaništšev, A. Ruzanov, K. Lust, E. Lust, J. Electrochem. Soc. 160 (2013) H368–H375.
[150] K. Lust, E. Lust, J. Electroanal. Chem. 552 (2003) 129–139.
[151] K. Lust, M. Väärtnõu, E. Lust, Electrochimica Acta. 45 (2000) 3543–3554.

[152] E.I. Rogers, I. Streeter, L. Aldous, C. Hardacre, R.G. Compton, J. Phys. Chem. C. 112 (2008) 10976–10981.
[153] V.K. Thorsmølle, G. Rothenberger, D. Topgaard, J.C. Brauer, D.-B. Kuang, S.M. Zakeeruddin, et al., ChemPhysChem. 12 (2011) 145–149.
[154] J. Hoth, F. Hausen, M.H. Müser, R. Bennewitz, J. Phys. Condens. Matter. 26 (2014) 284110.
[155] E. Lust, L. Siinor, H. Kurig, T. Romann, V. Ivaništšev, C. Siimenson, et al., ECS Trans. 75 (2016) 161–170.

9. SUMMARY IN ESTONIAN

Elektrilise kaksikkihi struktuur ja energia salvestamise karakteristikud ioonsetel vedelikel põhinevates kondensaatorites

Elektrokeemilised energia salvestamise ja muundamise seadmed on aluseks tuleviku jätkusuutlikule energiamajandusele. Olgu selleks siis elektromagnet kiirgust elektrienergiaks muundavad päikesepatareid, autotranspordis kasutatavad kütuseelemendid, veest kütust tootvad elektrolüüserid, sekundaar-akumulaatorid iga-päeva elektroonika-seadmetes, superkondensaatorid, mis säästavad energiat kõrge võimsusega rakendustes või dielektrilised kondensaatorid elektroonilistes muundurites, kõrgtehnoloogilised elektrokeemilised seadmed on kõikjal meie ümber. Kõikide eelpool nimetatud seadmete puhul on aktiivseks osaks kahe erineva materjali vaheline piirpind, kus toimuvad elektrokeemilised reaktsioonid ja salvestub elektrienergia. Uute, kõrge effektiivsusega elektrokeemiliste seadmete loomiseks on aga ülimalt oluline arusaam vastavat piirpinda mõjutavatest teguritest. Antud doktoritöö keskendub just mahtuvuslikele energia salvestamise seadmetele ja erinevustele elektrostaatiliste, dielektriliste ja pseudomahtuvuslike kondensaatorite vahel ioonse vedeliku ja elektroodi piirpinna vaheliste mõjude karakteriseerimise toel.

Aatomjõu mikroskoopia, tsüklilise voltamperomeetria, elektrokeemilise impedantsspektroskoopia ja *in situ* infrapuna neelduvus-spektroskoopia meetodeid rakendati elektrilise kaksikkihi (EKK) tekke ja laadimise protsesside uurimiseks viie erineva metallilisusega elektroodi materjali uurimiseks 1-etüül-3-metüülimidasoolium tetrafluoroboraadi ($EMImBF_4$) keskkonnas. Elektrokeemia mõõtmised näitavad, et EKK mahtuvus sõltub oluliselt elektroodimaterjali metallilistest omadustest. Spektroelektrokeemia mõõtmiste põhjal nähtub, et nii Au kui Pb puhul on meetod tundlik EKK kompaktse kihi suhtes, näidates ioonide kontsentratsiooni ja orientatsiooni muutuseid elektrokeemilise polarisatsiooni toimel. Pool-metalliliste omadustega Bi ja grafiidi puhul on meetod tundlik peamiselt EKK diffuusse kihi suhtes, näidates selles polarisatsiooni mõjul toimuvaid restruktureerumisi.

Arendati välja uudne kondensaatori tehnoloogia, mis põhineb elektropolümeriseeruvatel ditsüaanamiidi anioonidel. Näidati, et õhukesekihilised süsinikelektroodid on sobivad passiveerimiseks kuni 10 V-ni ditsüanamiidi sisaldavas ioonses vedelikus. Tõestati, et elektroodide pinnale tekkiv ühend on vaid süsiniku ja lämmastiku aatomitest koosnev polüditsüaanamiid (PDTA). Elektropeegelduse spektroskoopia tulemused näitavad, et energia salvestamise mehhanism vastavates grafiit│PDTA kondansaatorites erineb oluliselt ideaalselt polariseeritavast grafiit│$EMImBF_4$ elektrostaatilise kondensaatori puhul näidatud EKK laadimise mehhanismist.

EKK mahtuvuse ja piirpinna takistuse omadusi vaadeldi vaid jodiid anioone sisaldavas ioonses vedelikus kolmel erineva metallilisusega Bi monokristalli

piirpinnal. Näidati, et kuigi EKK mahtuvus sõltub oluliselt Bi monokristalli tahust, olles kõrgem metallilisemate tahkude korral, siis takistuslike parameetrite korral olulist kristallstruktuuri mõju ei täheldatud. Näidati, et EKK mahtuvus ioonses vedelikus jodiidiooni adsorptsiooni korral Bi(*hkl*) elektroodidele on äärmiselt sarnane suhteliselt lahja vesilahuse korral jodiidiooni adsorptsioonile samadele elektroodidele, mis on põhjustatud tugevast vastastikmõjust adsorbeerunud jodiidioonide ja metalli pindkihi vahel.

10. ACKNOWLEDGEMENTS

I would like to express my gratitude to my supervisors. Tavo has been a great example of what being a hard-working scientist is all about and I still have much to learn from him as an applied scientist. Enn, with his wealth of knowledge and experience, has allowed me to be and become the scientist that I wanted to, and I am extremely grateful for all the support throughout the years. Jovial discussions with him will always remind me that science is not always without laughter. The support of my first supervisor, Vladislav, is also greatly appreatiated. The positivity with which he carries himself has always been an admirable quality.

I would also like to thank my students, Georg and Jinfeng, who have made this journey more interesting and enjoyable. The great support from all the colleagues and coworkers through the years has been immensely important for both my personal and professional development. All the discussions, arguments and thought experiments have helped to shape my understanding of the world around us, and both inspired and motivated me on my scientific path. For this, I am extremely greatful to have had the opportunity to work alongside them.

The unwavering love and support by my family is truly the number one reason for me to be able to complete this part of the journey. Without them challenging me to become a better version of myself, this work would not have been feasible. Lastly, the continued support by my friends is greatly appreatiated.

This work was supported by the Estonian Ministry of Education and Research (projects no. IUT 20-13, PUT55, PUT1033 and PUT1107), and European Regional Development Fund (Estonian Centre of Excellence TK117T "High-technology Materials for Sustainable Development" and TK141 "Advanced materials and high-technology devices for energy recuperation systems"). This work has also been supported by ASTRA project PER ASPERA Graduate School of Functional Materials and Technologies receiving funding from the European Regional Development Fund under project at University of Tartu, Estonia.

Participation at scientific conferences was supported by national scholarship program Kristjan Jaak, which is funded and managed by Archimedes Foundation in collaboration with the Ministry of Education and Research.

11. PUBLICATIONS

CURRICULUM VITAE

Name: Ove Oll
Date of birth: March 15, 1990
Citizenship: Estonian
Contact: Institute of Chemistry, University of Tartu
Ravila 14A, 50411, Tartu, Estonia
E-mail: ove.oll@ut.ee

Education:

2014–…	University of Tartu, Institute of Chemistry – *Ph.D.* student
2013–2014	University of Tartu, Institute of Chemistry – *M.Sc.* Chemistry
2009–2013	University of Tartu, Institute of Chemistry – *B.Sc.* in Chemistry

Professional employment:

2012–…	University of Tartu, Institute of Chemistry, Chemist

Scientific organizations:

2015–…	Member of the International Society of Electrochemistry

List of publications:

1. T. Romann, **O. Oll**, P. Pikma, E. Lust, Abnormal infrared effects on bismuth thin film–EMImBF$_4$ ionic liquid interface, Electrochemistry Communications, 23, 118–121 (2012).
2. T. Romann, **O. Oll**, P. Pikma, H. Tamme, E. Lust, Surface chemistry of carbon electrodes in 1-ethyl-3-methylimidazolium tetrafluoroborate ionic liquid – an *in situ* infrared study, Electrochimica Acta, 125, 183–190 (2014).
3. **O. Oll,** T. Romann, E. Lust, An infrared study of the few-layer graphene │ionic liquid interface: Reintroduction of in situ electroreflectance spectroscopy, Electrochemistry Communications, 46, 22–25 (2014).
4. T. Romann, **O. Oll**, P. Pikma, K. Kirsimäe, E. Lust, 4–10 V capacitors with graphene-based electrodes and ionic liquid electrolyte, Journal of Power Sources, 280, 606–611 (2015).
5. P. Pikma, H. Kasuk, **O. Oll**, V. Ivaništšev, T. Romann, V. Grozovski, E. Lust, Adsorption of 4,4′-bipyridine on the Cd(0001) single crystal electrode surface, Electrochimica Acta, 180, 965−976 (2015).
6. P. Pikma, L. Siinor, **O. Oll**, E. Lust, Formation of 2,2′−bipyridine adlayers at Sb(111)│ionic liquid + 2,2′−bipyridine solution interface, Electrochemistry Communications, 61, 61−65 (2015).
7. C. Siimenson, M. Lembinen, **O. Oll**, L. Läll, M. Tarkanovskaja, V. Ivaništšev, L. Siinor, T. Thomberg, K. Lust, E. Lust, Electrochemical Investigation of 1-Ethyl-3-methylimidazolium Bromide and Tetrafluoroborate Mixture at Bi (111) Electrode Interface, Journal of The Electrochemical Society 163, no. 9, H723–H730 (2016).

8. E. Lust, L. Siinor, H. Kurig, T. Romann, V. Ivaništšev, C. Siimenson, … **O. Oll,** et al. Characteristics of Capacitors Based on Ionic Liquids: From Dielectric Polymers to Redox-Active Adsorbed Species, ECS Transactions, 75, no. 15, 161–170 (2016).
9. **O. Oll,** T. Romann, P. Pikma, E. Lust, Spectroscopy study of ionic liquid restructuring at lead interface, Journal of Electroanalytical Chemistry, 778, 41–48 (2016).
10. **O. Oll,** C. Siimenson, K. Lust, G. Gorbatovski, E. Lust, Specific adsorption from an ionic liquid: impedance study of iodide ion adsorption from a pure halide ionic liquid at bismuth single crystal planes, Electrochimica Acta, 247, 910–919 (2017).
11. **O. Oll,** T. Romann, C. Siimenson, E. Lust, Influence of chemical composition of electrode material on the differential capacitance characteristics of the ionic liquid│ electrode interface, Electrochemistry Communications, 82, 39–42 (2017).
12. R. Härmas, R. Palm, M. Härmas, M. Pohl, H. Kurig, I. Tallo, … **O. Oll**, et al. Influence of porosity parameters and electrolyte chemical composition on the power densities of non-aqueous and ionic liquid based supercapacitors, Electrochimica Acta (2018).

Industrial property:

1. T. Romann, E. Lust, **O. Oll**, Method of Forming a Dielectric Through Electrodeposition on an Electrode for a Capacitor, WO/2016/050761, 2016.

International conference presentations:

1. **Oll, Ove**; Romann, Tavo; Lust, Enn (2015). An Infrared Study of the Few-Layer Graphene | Ionic Liquid Interface: Correlation between Electronic and Ionic Surface Structure. 66th Annual Meeting of the International Society of Electrochemistry, Taipei, Taiwan, 4–9. October 2015.
2. **Oll, Ove**; Anderson, Erik; Siimenson, Carolin; Läll, Laura; Siinor, Liis; Lust, Enn; (2016). In Situ STM Studies of Electrochemical Stability and 2D Layer Formation at Bi(111)|Halide Ionic Liquid Mixture Interface. 67th Annual Meeting of the International Society of Electrochemistry, The Hague, The Netherlands, 21–26. August 2016.
3. Gorbatovski, Georg; Kasuk, Heili; **Oll, Ove**; Pikma, Piret; Lust, Enn; (2016). Formation of Bipyridine Self-Assembled Monolayers on Sb(111) Electrode Surface. 67th Annual Meeting of the International Society of Electrochemistry, The Hague, The Netherlands, 21–26. August 2016.
4. **Oll, Ove**; Siimenson, Carolin; Anderson, Erik; Gorbatovski, Georg; Lust, Enn; (2016). The Activity of Halide Ions and the Effect on the Electrochemical Stability of Bi (111) Electrode in a Mixture of Ionic Liquids. ECS Meeting Abstracts, 48: PRiME 2016, Honolulu, Hawaii, USA, 2–7. October 2016. USA: ECS Meeting Abstracts, 3572.
5. **Oll, Ove**; Gorbatovski, Georg; Anderson, Erik; Lust, Enn (2017). Specific Adsorption of Anions from Ionic Liquids: an in situ STM and Impedance

Study. 68th Annual Meeting of the International Society of Electrochemistry, Providence, Rhode Island, USA, 27. August–1. September 2017.

6. **Oll, Ove**; Romann, Tavo; Lust, Enn (2017). Electrosynthesis of cyano-group based dielectric films from ionic liquids. In: .2nd International Summer School "Multifunctional Smart Coatings and Surfaces", University of Aveiro, Aveiro, Portugal, 24–28. July 2017.
7. **Oll, Ove**; Lust, Enn (2018). Electroreflectance Study of Thin-film Graphite | Ionic Liquid Interface: Electro-optics of Electrical Double-Layer and Dielectric Capacitors. 22nd Topical Meeting of the International Society of Electrochemistry, Tokyo, Japan, 15–18. April 2018.

Supervision:

1. Georg Gorbatovski, Master's Degree, 2018, supervisors Enn Lust and Ove Oll, Electrochemical and *in situ* scanning tunneling microscopy study of Bi(*hkl*) │1-propyl-3-methylimidazolium iodide interface, University of Tartu.

ELULOOKIRJELDUS

Nimi: Ove Oll
Sünniaeg: 15. märts 1990
Kodakondsus: Eesti
Kontakt: Keemia Instituut, Tartu Ülikool
Ravila 14A, 50411, Tartu, Eesti
E-post: ove.oll@ut.ee

Haridus:

2014–...	Tartu Ülikool, Keemia Instituut – doktorant
2013–2014	Tartu Ülikool, Keemia Instituut – *M.Sc.* keemia erialal
2009–2013	Tartu Ülikool, Keemia Instituut – *B.Sc.* keemia erialal

Teenistuskäik:

2012–...	Tartu Ülikool, Keemia Instituut, keemik

Teadusorganisatsioonid:

2015–...	Rahvusvahelise elektrokeemiaühingu liige

Teaduspublikatsioonid:

1. T. Romann, **O. Oll**, P. Pikma, E. Lust, Abnormal infrared effects on bismuth thin film–EMImBF$_4$ ionic liquid interface, Electrochemistry Communications, 23, 118–121 (2012).
2. T. Romann, **O. Oll**, P. Pikma, H. Tamme, E. Lust, Surface chemistry of carbon electrodes in 1-ethyl-3-methylimidazolium tetrafluoroborate ionic liquid – an *in situ* infrared study, Electrochimica Acta, 125, 183–190 (2014).
3. **O. Oll,** T. Romann, E. Lust, An infrared study of the few-layer graphene│ionic liquid interface: Reintroduction of in situ electroreflectance spectroscopy, Electrochemistry Communications, 46, 22–25 (2014).
4. T. Romann, **O. Oll**, P. Pikma, K. Kirsimäe, E. Lust, 4–10 V capacitors with graphene-based electrodes and ionic liquid electrolyte, Journal of Power Sources, 280, 606–611 (2015).
5. P. Pikma, H. Kasuk, **O. Oll**, V. Ivaništšev, T. Romann, V. Grozovski, E. Lust, Adsorption of 4,4′-bipyridine on the Cd(0001) single crystal electrode surface, Electrochimica Acta, 180, 965−976 (2015).
6. P. Pikma, L. Siinor, **O. Oll**, E. Lust, Formation of 2,2′−bipyridine adlayers at Sb(111)│ionic liquid + 2,2′−bipyridine solution interface, Electrochemistry Communications, 61, 61−65 (2015).
7. C. Siimenson, M. Lembinen, **O. Oll**, L. Läll, M. Tarkanovskaja, V. Ivaništšev, L. Siinor, T. Thomberg, K. Lust, E. Lust, Electrochemical Investigation of 1-Ethyl-3-methylimidazolium Bromide and Tetrafluorobo-

rate Mixture at Bi (111) Electrode Interface, Journal of The Electrochemical Society 163, no. 9, H723–H730 (2016).

8. E. Lust, L. Siinor, H. Kurig, T. Romann, V. Ivaništšev, C. Siimenson, … **O. Oll,** et al. Characteristics of Capacitors Based on Ionic Liquids: From Dielectric Polymers to Redox-Active Adsorbed Species, ECS Transactions, 75, no. 15, 161–170 (2016).
9. **O. Oll,** T. Romann, P. Pikma, E. Lust, Spectroscopy study of ionic liquid restructuring at lead interface, Journal of Electroanalytical Chemistry, 778, 41-48 (2016).
10. **O. Oll,** C. Siimenson, K. Lust, G. Gorbatovski, E. Lust, Specific adsorption from an ionic liquid: impedance study of iodide ion adsorption from a pure halide ionic liquid at bismuth single crystal planes, Electrochimica Acta, 247, 910–919 (2017).
11. **O. Oll,** T. Romann, C. Siimenson, E. Lust, Influence of chemical composition of electrode material on the differential capacitance characteristics of the ionic liquid│ electrode interface, Electrochemistry Communications, 82, 39–42 (2017).
12. R. Härmas, R. Palm, M. Härmas, M. Pohl, H. Kurig, I. Tallo, … **O. Oll**, et al. Influence of porosity parameters and electrolyte chemical composition on the power densities of non-aqueous and ionic liquid based supercapacitors, Electrochimica Acta (2018).

Tööstusomand:

1. T. Romann, E. Lust, **O. Oll**, Method of Forming a Dielectric Through Electrodeposition on an Electrode for a Capacitor, WO/2016/050761, 2016.

Rahvusvahelised konverentsiettekanded:

1. **Oll, Ove**; Romann, Tavo; Lust, Enn (2015). An Infrared Study of the Few-Layer Graphene | Ionic Liquid Interface: Correlation between Electronic and Ionic Surface Structure. 66th Annual Meeting of the International Society of Electrochemistry, Taipei, Taiwan, 4–9. October 2015.
2. **Oll, Ove**; Anderson, Erik; Siimenson, Carolin; Läll, Laura; Siinor, Liis; Lust, Enn; (2016). In Situ STM Studies of Electrochemical Stability and 2D Layer Formation at Bi(111)|Halide Ionic Liquid Mixture Interface. 67th Annual Meeting of the International Society of Electrochemistry, The Hague, The Netherlands, 21–26. August 2016.
3. Gorbatovski, Georg; Kasuk, Heili; **Oll, Ove**; Pikma, Piret; Lust, Enn; (2016). Formation of Bipyridine Self-Assembled Monolayers on Sb(111) Electrode Surface. 67th Annual Meeting of the International Society of Electrochemistry, The Hague, The Netherlands, 21–26. August 2016.
4. **Oll, Ove**; Siimenson, Carolin; Anderson, Erik; Gorbatovski, Georg; Lust, Enn; (2016). The Activity of Halide Ions and the Effect on the Electrochemical Stability of Bi (111) Electrode in a Mixture of Ionic Liquids. ECS

Meeting Abstracts, 48: PRiME 2016, Honolulu, Hawaii, USA, 2–7. October 2016. USA: ECS Meeting Abstracts, 3572.

5. **Oll, Ove**; Gorbatovski, Georg; Anderson, Erik; Lust, Enn (2017). Specific Adsorption of Anions from Ionic Liquids: an in situ STM and Impedance Study. 68th Annual Meeting of the International Society of Electrochemistry, Providence, Rhode Island, USA, 27. August–1. September 2017.
6. **Oll, Ove**; Romann, Tavo; Lust, Enn (2017). Electrosynthesis of cyano-group based dielectric films from ionic liquids. In: .2nd International Summer School "Multifunctional Smart Coatings and Surfaces", University of Aveiro, Aveiro, Portugal, 24–28. July 2017.
7. **Oll, Ove**; Lust, Enn (2018). Electroreflectance Study of Thin-film Graphite | Ionic Liquid Interface: Electro-optics of Electrical Double-Layer and Dielectric Capacitors. 22nd Topical Meeting of the International Society of Electrochemistry, Tokyo, Japan, 15–18. April 2018.

Juhendamised:

1. Georg Gorbatovski, Magistrikraad, 2018, juhendajad Enn Lust ja Ove Oll, Electrochemical and *in situ* scanning tunneling microscopy study of Bi(*hkl*) │ 1-propyl-3-methylimidazolium iodide interface, Tartu Ülikool

DISSERTATIONES CHIMICAE UNIVERSITATIS TARTUENSIS

1. **Toomas Tamm.** Quantum-chemical simulation of solvent effects. Tartu, 1993, 110 p.
2. **Peeter Burk.** Theoretical study of gas-phase acid-base equilibria. Tartu, 1994, 96 p.
3. **Victor Lobanov.** Quantitative structure-property relationships in large descriptor spaces. Tartu, 1995, 135 p.
4. **Vahur Mäemets.** The ^{17}O and ^{1}H nuclear magnetic resonance study of H_2O in individual solvents and its charged clusters in aqueous solutions of electrolytes. Tartu, 1997, 140 p.
5. **Andrus Metsala.** Microcanonical rate constant in nonequilibrium distribution of vibrational energy and in restricted intramolecular vibrational energy redistribution on the basis of slater's theory of unimolecular reactions. Tartu, 1997, 150 p.
6. **Uko Maran.** Quantum-mechanical study of potential energy surfaces in different environments. Tartu, 1997, 137 p.
7. **Alar Jänes.** Adsorption of organic compounds on antimony, bismuth and cadmium electrodes. Tartu, 1998, 219 p.
8. **Kaido Tammeveski.** Oxygen electroreduction on thin platinum films and the electrochemical detection of superoxide anion. Tartu, 1998, 139 p.
9. **Ivo Leito.** Studies of Brønsted acid-base equilibria in water and non-aqueous media. Tartu, 1998, 101 p.
10. **Jaan Leis.** Conformational dynamics and equilibria in amides. Tartu, 1998, 131 p.
11. **Toonika Rinken.** The modelling of amperometric biosensors based on oxidoreductases. Tartu, 2000, 108 p.
12. **Dmitri Panov.** Partially solvated Grignard reagents. Tartu, 2000, 64 p.
13. **Kaja Orupõld.** Treatment and analysis of phenolic wastewater with microorganisms. Tartu, 2000, 123 p.
14. **Jüri Ivask.** Ion Chromatographic determination of major anions and cations in polar ice core. Tartu, 2000, 85 p.
15. **Lauri Vares.** Stereoselective Synthesis of Tetrahydrofuran and Tetrahydropyran Derivatives by Use of Asymmetric Horner-Wadsworth-Emmons and Ring Closure Reactions. Tartu, 2000, 184 p.
16. **Martin Lepiku.** Kinetic aspects of dopamine D_2 receptor interactions with specific ligands. Tartu, 2000, 81 p.
17. **Katrin Sak.** Some aspects of ligand specificity of P2Y receptors. Tartu, 2000, 106 p.
18. **Vello Pällin.** The role of solvation in the formation of iotsitch complexes. Tartu, 2001, 95 p.
19. **Katrin Kollist.** Interactions between polycyclic aromatic compounds and humic substances. Tartu, 2001, 93 p.

20. **Ivar Koppel.** Quantum chemical study of acidity of strong and superstrong Brønsted acids. Tartu, 2001, 104 p.
21. **Viljar Pihl.** The study of the substituent and solvent effects on the acidity of OH and CH acids. Tartu, 2001, 132 p.
22. **Natalia Palm.** Specification of the minimum, sufficient and significant set of descriptors for general description of solvent effects. Tartu, 2001, 134 p.
23. **Sulev Sild.** QSPR/QSAR approaches for complex molecular systems. Tartu, 2001, 134 p.
24. **Ruslan Petrukhin.** Industrial applications of the quantitative structure-property relationships. Tartu, 2001, 162 p.
25. **Boris V. Rogovoy.** Synthesis of (benzotriazolyl)carboximidamides and their application in relations with *N*- and *S*-nucleophyles. Tartu, 2002, 84 p.
26. **Koit Herodes.** Solvent effects on UV-vis absorption spectra of some solvatochromic substances in binary solvent mixtures: the preferential solvation model. Tartu, 2002, 102 p.
27. **Anti Perkson.** Synthesis and characterisation of nanostructured carbon. Tartu, 2002, 152 p.
28. **Ivari Kaljurand.** Self-consistent acidity scales of neutral and cationic Brønsted acids in acetonitrile and tetrahydrofuran. Tartu, 2003, 108 p.
29. **Karmen Lust.** Adsorption of anions on bismuth single crystal electrodes. Tartu, 2003, 128 p.
30. **Mare Piirsalu.** Substituent, temperature and solvent effects on the alkaline hydrolysis of substituted phenyl and alkyl esters of benzoic acid. Tartu, 2003, 156 p.
31. **Meeri Sassian.** Reactions of partially solvated Grignard reagents. Tartu, 2003, 78 p.
32. **Tarmo Tamm.** Quantum chemical modelling of polypyrrole. Tartu, 2003. 100 p.
33. **Erik Teinemaa.** The environmental fate of the particulate matter and organic pollutants from an oil shale power plant. Tartu, 2003. 102 p.
34. **Jaana Tammiku-Taul.** Quantum chemical study of the properties of Grignard reagents. Tartu, 2003. 120 p.
35. **Andre Lomaka.** Biomedical applications of predictive computational chemistry. Tartu, 2003. 132 p.
36. **Kostyantyn Kirichenko.** Benzotriazole – Mediated Carbon–Carbon Bond Formation. Tartu, 2003. 132 p.
37. **Gunnar Nurk.** Adsorption kinetics of some organic compounds on bismuth single crystal electrodes. Tartu, 2003, 170 p.
38. **Mati Arulepp.** Electrochemical characteristics of porous carbon materials and electrical double layer capacitors. Tartu, 2003, 196 p.
39. **Dan Cornel Fara.** QSPR modeling of complexation and distribution of organic compounds. Tartu, 2004, 126 p.
40. **Riina Mahlapuu.** Signalling of galanin and amyloid precursor protein through adenylate cyclase. Tartu, 2004, 124 p.

41. **Mihkel Kerikmäe.** Some luminescent materials for dosimetric applications and physical research. Tartu, 2004, 143 p.
42. **Jaanus Kruusma.** Determination of some important trace metal ions in human blood. Tartu, 2004, 115 p.
43. **Urmas Johanson.** Investigations of the electrochemical properties of polypyrrole modified electrodes. Tartu, 2004, 91 p.
44. **Kaido Sillar.** Computational study of the acid sites in zeolite ZSM-5. Tartu, 2004, 80 p.
45. **Aldo Oras.** Kinetic aspects of dATPαS interaction with $P2Y_1$ receptor. Tartu, 2004, 75 p.
46. **Erik Mölder.** Measurement of the oxygen mass transfer through the air-water interface. Tartu, 2005, 73 p.
47. **Thomas Thomberg.** The kinetics of electroreduction of peroxodisulfate anion on cadmium (0001) single crystal electrode. Tartu, 2005, 95 p.
48. **Olavi Loog.** Aspects of condensations of carbonyl compounds and their imine analogues. Tartu, 2005, 83 p.
49. **Siim Salmar.** Effect of ultrasound on ester hydrolysis in aqueous ethanol. Tartu, 2006, 73 p.
50. **Ain Uustare.** Modulation of signal transduction of heptahelical receptors by other receptors and G proteins. Tartu, 2006, 121 p.
51. **Sergei Yurchenko.** Determination of some carcinogenic contaminants in food. Tartu, 2006, 143 p.
52. **Kaido Tämm.** QSPR modeling of some properties of organic compounds. Tartu, 2006, 67 p.
53. **Olga Tšubrik.** New methods in the synthesis of multisubstituted hydrazines. Tartu. 2006, 183 p.
54. **Lilli Sooväli.** Spectrophotometric measurements and their uncertainty in chemical analysis and dissociation constant measurements. Tartu, 2006, 125 p.
55. **Eve Koort.** Uncertainty estimation of potentiometrically measured ph and pK_a values. Tartu, 2006, 139 p.
56. **Sergei Kopanchuk.** Regulation of ligand binding to melanocortin receptor subtypes. Tartu, 2006, 119 p.
57. **Silvar Kallip.** Surface structure of some bismuth and antimony single crystal electrodes. Tartu, 2006, 107 p.
58. **Kristjan Saal.** Surface silanization and its application in biomolecule coupling. Tartu, 2006, 77 p.
59. **Tanel Tätte.** High viscosity $Sn(OBu)_4$ oligomeric concentrates and their applications in technology. Tartu, 2006, 91 p.
60. **Dimitar Atanasov Dobchev**. Robust QSAR methods for the prediction of properties from molecular structure. Tartu, 2006, 118 p.
61. **Hannes Hagu**. Impact of ultrasound on hydrophobic interactions in solutions. Tartu, 2007, 81 p.
62. **Rutha Jäger.** Electroreduction of peroxodisulfate anion on bismuth electrodes. Tartu, 2007, 142 p.

63. **Kaido Viht.** Immobilizable bisubstrate-analogue inhibitors of basophilic protein kinases: development and application in biosensors. Tartu, 2007, 88 p.
64. **Eva-Ingrid Rõõm.** Acid-base equilibria in nonpolar media. Tartu, 2007, 156 p.
65. **Sven Tamp.** DFT study of the cesium cation containing complexes relevant to the cesium cation binding by the humic acids. Tartu, 2007, 102 p.
66. **Jaak Nerut.** Electroreduction of hexacyanoferrate(III) anion on Cadmium (0001) single crystal electrode. Tartu, 2007, 180 p.
67. **Lauri Jalukse.** Measurement uncertainty estimation in amperometric dissolved oxygen concentration measurement. Tartu, 2007, 112 p.
68. **Aime Lust.** Charge state of dopants and ordered clusters formation in CaF_2:Mn and CaF_2:Eu luminophors. Tartu, 2007, 100 p.
69. **Iiris Kahn**. Quantitative Structure-Activity Relationships of environmentally relevant properties. Tartu, 2007, 98 p.
70. **Mari Reinik.** Nitrates, nitrites, N-nitrosamines and polycyclic aromatic hydrocarbons in food: analytical methods, occurrence and dietary intake. Tartu, 2007, 172 p.
71. **Heili Kasuk.** Thermodynamic parameters and adsorption kinetics of organic compounds forming the compact adsorption layer at Bi single crystal electrodes. Tartu, 2007, 212 p.
72. **Erki Enkvist.** Synthesis of adenosine-peptide conjugates for biological applications. Tartu, 2007, 114 p.
73. **Svetoslav Hristov Slavov**. Biomedical applications of the QSAR approach. Tartu, 2007, 146 p.
74. **Eneli Härk.** Electroreduction of complex cations on electrochemically polished Bi(*hkl*) single crystal electrodes. Tartu, 2008, 158 p.
75. **Priit Möller.** Electrochemical characteristics of some cathodes for medium temperature solid oxide fuel cells, synthesized by solid state reaction technique. Tartu, 2008, 90 p.
76. **Signe Viggor.** Impact of biochemical parameters of genetically different pseudomonads at the degradation of phenolic compounds. Tartu, 2008, 122 p.
77. **Ave Sarapuu.** Electrochemical reduction of oxygen on quinone-modified carbon electrodes and on thin films of platinum and gold. Tartu, 2008, 134 p.
78. **Agnes Kütt.** Studies of acid-base equilibria in non-aqueous media. Tartu, 2008, 198 p.
79. **Rouvim Kadis.** Evaluation of measurement uncertainty in analytical chemistry: related concepts and some points of misinterpretation. Tartu, 2008, 118 p.
80. **Valter Reedo.** Elaboration of IVB group metal oxide structures and their possible applications. Tartu, 2008, 98 p.
81. **Aleksei Kuznetsov.** Allosteric effects in reactions catalyzed by the cAMP-dependent protein kinase catalytic subunit. Tartu, 2009, 133 p.

82. **Aleksei Bredihhin.** Use of mono- and polyanions in the synthesis of multisubstituted hydrazine derivatives. Tartu, 2009, 105 p.
83. **Anu Ploom.** Quantitative structure-reactivity analysis in organosilicon chemistry. Tartu, 2009, 99 p.
84. **Argo Vonk.** Determination of adenosine A_{2A}- and dopamine D_1 receptor-specific modulation of adenylate cyclase activity in rat striatum. Tartu, 2009, 129 p.
85. **Indrek Kivi.** Synthesis and electrochemical characterization of porous cathode materials for intermediate temperature solid oxide fuel cells. Tartu, 2009, 177 p.
86. **Jaanus Eskusson.** Synthesis and characterisation of diamond-like carbon thin films prepared by pulsed laser deposition method. Tartu, 2009, 117 p.
87. **Marko Lätt.** Carbide derived microporous carbon and electrical double layer capacitors. Tartu, 2009, 107 p.
88. **Vladimir Stepanov.** Slow conformational changes in dopamine transporter interaction with its ligands. Tartu, 2009, 103 p.
89. **Aleksander Trummal.** Computational Study of Structural and Solvent Effects on Acidities of Some Brønsted Acids. Tartu, 2009, 103 p.
90. **Eerold Vellemäe.** Applications of mischmetal in organic synthesis. Tartu, 2009, 93 p.
91. **Sven Parkel.** Ligand binding to 5-HT_{1A} receptors and its regulation by Mg^{2+} and Mn^{2+}. Tartu, 2010, 99 p.
92. **Signe Vahur.** Expanding the possibilities of ATR-FT-IR spectroscopy in determination of inorganic pigments. Tartu, 2010, 184 p.
93. **Tavo Romann**. Preparation and surface modification of bismuth thin film, porous, and microelectrodes. Tartu, 2010, 155 p.
94. **Nadežda Aleksejeva.** Electrocatalytic reduction of oxygen on carbon nanotube-based nanocomposite materials. Tartu, 2010, 147 p.
95. **Marko Kullapere.** Electrochemical properties of glassy carbon, nickel and gold electrodes modified with aryl groups. Tartu, 2010, 233 p.
96. **Liis Siinor.** Adsorption kinetics of ions at Bi single crystal planes from aqueous electrolyte solutions and room-temperature ionic liquids. Tartu, 2010, 101 p.
97. **Angela Vaasa.** Development of fluorescence-based kinetic and binding assays for characterization of protein kinases and their inhibitors. Tartu 2010, 101 p.
98. **Indrek Tulp.** Multivariate analysis of chemical and biological properties. Tartu 2010, 105 p.
99. **Aare Selberg.** Evaluation of environmental quality in Northern Estonia by the analysis of leachate. Tartu 2010, 117 p.
100. **Darja Lavõgina.** Development of protein kinase inhibitors based on adenosine analogue-oligoarginine conjugates. Tartu 2010, 248 p.
101. **Laura Herm.** Biochemistry of dopamine D_2 receptors and its association with motivated behaviour. Tartu 2010, 156 p.

102. **Terje Raudsepp.** Influence of dopant anions on the electrochemical properties of polypyrrole films. Tartu 2010, 112 p.
103. **Margus Marandi.** Electroformation of Polypyrrole Films: *In-situ* AFM and STM Study. Tartu 2011, 116 p.
104. **Kairi Kivirand.** Diamine oxidase-based biosensors: construction and working principles. Tartu, 2011, 140 p.
105. **Anneli Kruve.** Matrix effects in liquid-chromatography electrospray mass-spectrometry. Tartu, 2011, 156 p.
106. **Gary Urb.** Assessment of environmental impact of oil shale fly ash from PF and CFB combustion. Tartu, 2011, 108 p.
107. **Nikita Oskolkov.** A novel strategy for peptide-mediated cellular delivery and induction of endosomal escape. Tartu, 2011, 106 p.
108. **Dana Martin.** The QSPR/QSAR approach for the prediction of properties of fullerene derivatives. Tartu, 2011, 98 p.
109. **Säde Viirlaid.** Novel glutathione analogues and their antioxidant activity. Tartu, 2011, 106 p.
110. **Ülis Sõukand.** Simultaneous adsorption of Cd^{2+}, Ni^{2+}, and Pb^{2+} on peat. Tartu, 2011, 124 p.
111. **Lauri Lipping.** The acidity of strong and superstrong Brønsted acids, an outreach for the "limits of growth": a quantum chemical study. Tartu, 2011, 124 p.
112. **Heisi Kurig.** Electrical double-layer capacitors based on ionic liquids as electrolytes. Tartu, 2011, 146 p.
113. **Marje Kasari.** Bisubstrate luminescent probes, optical sensors and affinity adsorbents for measurement of active protein kinases in biological samples. Tartu, 2012, 126 p.
114. **Kalev Takkis.** Virtual screening of chemical databases for bioactive molecules. Tartu, 2012, 122 p.
115. **Ksenija Kisseljova**. Synthesis of aza-β^3-amino acid containing peptides and kinetic study of their phosphorylation by protein kinase A. Tartu, 2012, 104 p.
116. **Riin Rebane.** Advanced method development strategy for derivatization LC/ESI/MS. Tartu, 2012, 184 p.
117. **Vladislav Ivaništšev.** Double layer structure and adsorption kinetics of ions at metal electrodes in room temperature ionic liquids. Tartu, 2012, 128 p.
118. **Irja Helm.** High accuracy gravimetric Winkler method for determination of dissolved oxygen. Tartu, 2012, 139 p.
119. **Karin Kipper.** Fluoroalcohols as Components of LC-ESI-MS Eluents: Usage and Applications. Tartu, 2012, 164 p.
120. **Arno Ratas.** Energy storage and transfer in dosimetric luminescent materials. Tartu, 2012, 163 p.
121. **Reet Reinart-Okugbeni**. Assay systems for characterisation of subtype-selective binding and functional activity of ligands on dopamine receptors. Tartu, 2012, 159 p.

122. **Lauri Sikk.** Computational study of the Sonogashira cross-coupling reaction. Tartu, 2012, 81 p.
123. **Karita Raudkivi.** Neurochemical studies on inter-individual differences in affect-related behaviour of the laboratory rat. Tartu, 2012, 161 p.
124. **Indrek Saar.** Design of GalR2 subtype specific ligands: their role in depression-like behavior and feeding regulation. Tartu, 2013, 126 p.
125. **Ann Laheäär.** Electrochemical characterization of alkali metal salt based non-aqueous electrolytes for supercapacitors. Tartu, 2013, 127 p.
126. **Kerli Tõnurist.** Influence of electrospun separator materials properties on electrochemical performance of electrical double-layer capacitors. Tartu, 2013, 147 p.
127. **Kaija Põhako-Esko.** Novel organic and inorganic ionogels: preparation and characterization. Tartu, 2013, 124 p.
128. **Ivar Kruusenberg.** Electroreduction of oxygen on carbon nanomaterial-based catalysts. Tartu, 2013, 191 p.
129. **Sander Piiskop.** Kinetic effects of ultrasound in aqueous acetonitrile solutions. Tartu, 2013, 95 p.
130. **Ilona Faustova**. Regulatory role of L-type pyruvate kinase N-terminal domain. Tartu, 2013, 109 p.
131. **Kadi Tamm.** Synthesis and characterization of the micro-mesoporous anode materials and testing of the medium temperature solid oxide fuel cell single cells. Tartu, 2013, 138 p.
132. **Iva Bozhidarova Stoyanova-Slavova.** Validation of QSAR/QSPR for regulatory purposes. Tartu, 2013, 109 p.
133. **Vitali Grozovski**. Adsorption of organic molecules at single crystal electrodes studied by *in situ* STM method. Tartu, 2014, 146 p.
134. **Santa Veikšina**. Development of assay systems for characterisation of ligand binding properties to melanocortin 4 receptors. Tartu, 2014, 151 p.
135. **Jüri Liiv.** PVDF (polyvinylidene difluoride) as material for active element of twisting-ball displays. Tartu, 2014, 111 p.
136. **Kersti Vaarmets.** Electrochemical and physical characterization of pristine and activated molybdenum carbide-derived carbon electrodes for the oxygen electroreduction reaction. Tartu, 2014, 131 p.
137. **Lauri Tõntson**. Regulation of G-protein subtypes by receptors, guanine nucleotides and Mn^{2+}. Tartu, 2014, 105 p.
138. **Aiko Adamson.** Properties of amine-boranes and phosphorus analogues in the gas phase. Tartu, 2014, 78 p.
139. **Elo Kibena**. Electrochemical grafting of glassy carbon, gold, highly oriented pyrolytic graphite and chemical vapour deposition-grown graphene electrodes by diazonium reduction method. Tartu, 2014, 184 p.
140. **Teemu Näykki.** Novel Tools for Water Quality Monitoring – From Field to Laboratory. Tartu, 2014, 202 p.
141. **Karl Kaupmees.** Acidity and basicity in non-aqueous media: importance of solvent properties and purity. Tartu, 2014, 128 p.

142. **Oleg Lebedev**. Hydrazine polyanions: different strategies in the synthesis of heterocycles. Tartu, 2015, 118 p.
143. **Geven Piir.** Environmental risk assessment of chemicals using QSAR methods. Tartu, 2015, 123 p.
144. **Olga Mazina.** Development and application of the biosensor assay for measurements of cyclic adenosine monophosphate in studies of G protein-coupled receptor signalinga. Tartu, 2015, 116 p.
145. **Sandip Ashokrao Kadam.** Anion receptors: synthesis and accurate binding measurements. Tartu, 2015, 116 p.
146. **Indrek Tallo.** Synthesis and characterization of new micro-mesoporous carbide derived carbon materials for high energy and power density electrical double layer capacitors. Tartu, 2015, 148 p.
147. **Heiki Erikson.** Electrochemical reduction of oxygen on nanostructured palladium and gold catalysts. Tartu, 2015, 204 p.
148. **Erik Anderson.** *In situ* Scanning Tunnelling Microscopy studies of the interfacial structure between Bi(111) electrode and a room temperature ionic liquid. Tartu, 2015, 118 p.
149. **Girinath G. Pillai.** Computational Modelling of Diverse Chemical, Bio-chemical and Biomedical Properties. Tartu, 2015, 140 p.
150. **Piret Pikma.** Interfacial structure and adsorption of organic compounds at Cd(0001) and Sb(111) electrodes from ionic liquid and aqueous electrolytes: an *in situ* STM study. Tartu, 2015, 126 p.
151. **Ganesh babu Manoharan.** Combining chemical and genetic approaches for photoluminescence assays of protein kinases. Tartu, 2016, 126 p.
152. **Carolin Siimenson**. Electrochemical characterization of halide ion adsorption from liquid mixtures at Bi(111) and pyrolytic graphite electrode surface. Tartu, 2016, 110 p.
153. **Asko Laaniste.** Comparison and optimisation of novel mass spectrometry ionisation sources. Tartu, 2016, 156 p.
154. **Hanno Evard.** Estimating limit of detection for mass spectrometric analysis methods. Tartu, 2016, 224 p.
155. **Kadri Ligi.** Characterization and application of protein kinase-responsive organic probes with triplet-singlet energy transfer. Tartu, 2016, 122 p.
156. **Margarita Kagan.** Biosensing penicillins' residues in milk flows. Tartu, 2016, 130 p.
157. **Marie Kriisa.** Development of protein kinase-responsive photo-luminescent probes and cellular regulators of protein phosphorylation. Tartu, 2016, 106 p.
158. **Mihkel Vestli.** Ultrasonic spray pyrolysis deposited electrolyte layers for intermediate temperature solid oxide fuel cells. Tartu, 2016, 156 p.
159. **Silver Sepp**. Influence of porosity of the carbide-derived carbon on the properties of the composite electrocatalysts and characteristics of polymer electrolyte fuel cells. Tartu, 2016, 137p.
160. **Kristjan Haav**. Quantitative relative equilibrium constant measurements in supramolecular chemistry. Tartu, 2017, 158 p.

161. **Anu Teearu**. Development of MALDI-FT-ICR-MS methodology for the analysis of resinous materials. Tartu, 2017, 205 p.
162. **Taavi Ivan**. Bifunctional inhibitors and photoluminescent probes for studies on protein complexes. Tartu, 2017, 140 p.
163. **Maarja-Liisa Oldekop**. Characterization of amino acid derivatization reagents for LC-MS analysis. Tartu, 2017, 147 p.
164. **Kristel Jukk**. Electrochemical reduction of oxygen on platinum- and palladium-based nanocatalysts. Tartu, 2017, 250 p.
165. **Siim Kukk**. Kinetic aspects of interaction between dopamine transporter and *N*-substituted nortropane derivatives. Tartu, 2017, 107 p.
166. **Birgit Viira**. Design and modelling in early drug development in targeting HIV-1 reverse transcriptase and Malaria. Tartu, 2017, 172 p.
167. **Rait Kivi**. Allostery in cAMP dependent protein kinase catalytic subunit. Tartu, 2017, 115 p.
168. **Agnes Heering**. Experimental realization and applications of the unified acidity scale. Tartu, 2017, 123 p.
169. **Delia Juronen**. Biosensing system for the rapid multiplex detection of mastitis-causing pathogens in milk. Tartu, 2018, 85 p.
170. **Hedi Rahnel.** ARC-inhibitors: from reliable biochemical assays to regulators of physiology of cells. Tartu, 2018, 176 p.
171. **Anton Ruzanov.** Computational investigation of the electrical double layer at metal–aqueous solution and metal–ionic liquid interfaces. Tartu, 2018, 129 p.
172. **Katrin Kestav.** Crystal Structure-Guided Development of Bisubstrate-Analogue Inhibitors of Mitotic Protein Kinase Haspin. Tartu, 2018, 166 p.
173. **Mihkel Ilisson.** Synthesis of novel heterocyclic hydrazine derivatives and their conjugates. Tartu, 2018, 101 p.
174. **Anni Allikalt.** Development of assay systems for studying ligand binding to dopamine receptors. Tartu, 2018, 160 p.